

MS 66733R revised 28-09-2018

1 **A terrestrial magmatic hibonite-grossite-vanadium assemblage: desilication**
2 **and extreme reduction in a volcanic plumbing system, Mt Carmel, Israel**

3
4 William L. GRIFFIN¹, Sarah E.M. GAIN¹, Jin-Xiang HUANG¹, Martin SAUNDERS²,
5 Jeremy SHAW², Vered TOLEDO³ and Suzanne Y. O'REILLY¹

6
7 ¹*ARC Centre of Excellence for Core to Crust Fluid Systems (CCFS) and GEMOC,*
8 *Earth and Planetary Sciences, Macquarie University, NSW 2109, Australia;*

9 bill.griffin@mq.edu.au

10 ²*Centre for Microscopy, Characterisation and Analysis, The University of Western*
11 *Australia, WA 6009, Australia; martin.saunders@uwa.edu.au*

12 ³*Shefa Yamim (A.T.M.) Ltd., Netanya 4210602, Israel; vered@shefayamim.com*

13
14 **Abstract**

15 Hibonite (CaAl₁₂O₁₉) is a constituent of some refractory Calcium-Aluminum
16 Inclusions (CAIs) in carbonaceous meteorites, commonly accompanied by grossite
17 (CaAl₄O₇) and spinel. These phases are usually interpreted as having condensed, or
18 crystallized from silicate melts, early in the evolution of the solar nebula. Both Ca-Al
19 oxides are commonly found on Earth, but as products of high-temperature
20 metamorphism of pelitic carbonate rocks. We report here a unique occurrence of
21 magmatic hibonite-grossite-spinel assemblages, crystallized from Ca-Al-rich silicate
22 melts under conditions (high temperature, very low oxygen fugacity (fO_2))
23 comparable to those of their meteoritic counterparts. Ejecta from Cretaceous
24 pyroclastic deposits on Mt Carmel, N. Israel, include aggregates of hopper/skeletal
25 Ti-rich corundum, which have trapped melts that crystallized at fO_2 extending from 7
26 log units below the Iron-Wustite buffer ($\Delta IW = -7$; SiC, Ti₂O₃, Fe-Ti silicide melts) to
27 $\Delta IW \leq -9$ (native V, TiC, TiN). The assemblage hibonite+grossite+spinel+TiN first
28 crystallized late in the evolution of the melt pockets; this hibonite contains % levels of
29 Zr, Ti and REE, reflecting the concentration of incompatible elements in the residual
30 melts as corundum continued to crystallize. A still later stage appears to be
31 represented by coarse-grained (cm-size crystals) ejecta that show the crystallization
32 sequence: corundum + Liq → (low-REE) hibonite → grossite + spinel ± krotite →
33 Ca₄Al₆F₂O₁₂ + fluorite. V⁰ appears as spheroidal droplets, balls up to mm size, and

MS 66733R revised 28-09-2018

34 spectacular dendritic growths, included in hibonite, grossite and spinel. Texturally
35 late V^0 averages 12 wt% Al and 2 wt% Mn. Spinels contain 10-16 wt% V in V^0 -free
36 samples, and <0.5 wt% V in samples with abundant V^0 . Ongoing paragenetic
37 studies suggest that the fO_2 evolution of the Mt Carmel magmatic system reflects
38 interaction between OIB-type mafic magmas and mantle-derived CH_4+H_2 fluids near
39 the crust-mantle boundary. Temperatures estimated by comparison with 1-atm.
40 phase-equilibrium studies range from ca 1500 °C down to 1200-1150 °C. When fO_2
41 reached ca $\Delta IW = -7$, the immiscible segregation of Fe,Ti-silicide melts and the
42 crystallization of SiC and TiC effectively desilicated the magma, leading to
43 supersaturation in Al_2O_3 and the rapid crystallization of corundum, preceding the
44 development of the hibonite-bearing assemblages. Reports of Ti-rich corundum and
45 SiC from other areas of explosive volcanism suggest that these phenomena may be
46 more widespread than presently realized, and the hibonite-grossite assemblage may
47 serve as another indicator to track such activity.
48 This is the first reported terrestrial occurrence of krotite ($CaAl_2O_4$), and of at least two
49 unknown Zr-Ti oxides.

50

51 **Introduction**

52 Hibonite ($CaAl_{12}O_{19}$) was described as a new mineral in 1956 (Curien et al.,
53 1956), and is named after Paul Hibon, who found cm-sized black crystals in a placer
54 deposit in Madagascar in 1953. It is a constituent of some refractory Calcium-
55 Aluminum Inclusions (CAIs) in carbonaceous chondrites, commonly associated with
56 grossite ($CaAl_4O_7$) and corundum (Grossman et al., 1988; Beckett et al., 2006).
57 Hibonite also occurs as microscopic grains in meteorites and it is one of the oldest
58 minerals in the solar system.

59 The type locality of hibonite is the Esiva alluvial deposits, in Tulear Province,
60 Madagascar. The material was probably derived from nearby deposits of thorianite-
61 bearing skarns, which are widespread in the Pan-African (565-515 Ma) granulite
62 belts of Madagascar and Tanzania (Rakotondrazafy et al., 1996). In these rocks,
63 early corundum + spinel + scapolite assemblages are altered to anorthite + calcite +
64 less calcic scapolite, while hibonite crystallized at the expense of corundum and
65 spinel. Hibonite also occurs as tabular crystals up to 3 cm across in calcitic marbles
66 from the Tashelga-Malzaskaya region in Siberia (Konovalenko et al., 2012). These

MS 66733R revised 28-09-2018

67 metamorphic hibonites are notably high in Fe^{3+} , and coexist with V-rich minerals
68 (goldmanite, tashelgite, mukhinite). P-T conditions are estimated at 700-800 °C, 3.5
69 kbar. The crystallization of hibonite implies a very low silica activity and, in this
70 location, probably high CO_2 .

71 The type locality of grossite is the Hatrurim formation (formerly known as the
72 “Mottled Zone”), a unique rock complex exposed mainly in the Judean Desert of
73 Israel, where it was first described by Gross (1977). The formation was deposited as
74 a thin marine, bituminous chalk-marl formation of Campanian to Neogene age.
75 However, at several localities, it is metamorphosed to the sanidinite and pyroxene-
76 hornfels facies (up to 1000 °C, very low P), due to spontaneous isochemical
77 combustion of bituminous compounds. Hibonite and grossite are widespread in these
78 metamorphosed sediments.

79 All previously known terrestrial occurrences of hibonite and grossite are, to
80 our knowledge, metamorphic in origin. In contrast, the textures of hibonite-bearing
81 CAIs in CV chondrites are ambiguous; hibonite occurs as a minor phase coexisting
82 with melilite, or in coarse-grained assemblages that could be metamorphic.
83 However, CAIs from CM chondrites are dominated by assemblages such as
84 hibonite+ spinel + perovskite, some of which contain glass. Textural features are
85 consistent with crystallization of hibonite from Al-rich melts (Kurat, 1975; Grossman
86 et al., 1988; Ireland et al., 1991), condensed from the solar nebula. The predicted
87 sequence of crystallization would be corundum-hibonite-perovskite, with subsequent
88 reactions leading to melilite and spinel. The condensation and crystallization of such
89 melts would require temperatures of ca 1500 - 1300 °C and would have occurred at
90 the very low oxygen fugacity ($f\text{O}_2$) imposed by the hydrogen-dominated composition
91 of the early solar nebula (Yoneda and Grossman, 1995; Grossman et al., 2008).

92 The apparent absence of magmatic hibonite-grossite assemblages on Earth
93 thus is understandable. However, we report here a terrestrial analog to the hibonite-
94 bearing CAIs of CM chondrites, from the Mt Carmel volcanics of northern Israel. Our
95 aim is to document these unusual parageneses; define their relationships to other
96 members of the ultra-reduced Mt Carmel volcanic system (Griffin et al., 2016, 2018;
97 Xiong et al., 2017); discuss briefly the mechanisms that can produce similar high-T,
98 low- $f\text{O}_2$ environments on Earth and indicate its implications for the behaviour of
99 carbon in deep-seated volcanic systems.

100

MS 66733R revised 28-09-2018

101

102 **Background**

103 Several years of exploration for placer gemstone deposits in the drainage of
104 the Kishon river, which enters the sea near Haifa in northern Israel (Fig. SD1), have
105 provided this unusual occurrence of hibonite and grossite.

106 Upper Cretaceous (98-80 Ma, Turonian-Cenomanian) mafic to ultramafic
107 pyroclastic rocks (vent breccias, tuffs) exposed in the Mt Carmel area, northern
108 Israel, represent a series of small explosive volcanoes that erupted on a shallow
109 carbonate shelf (Sass, 1980). Black pyroclastics occur in eruptive vents, while
110 variegated pyroclastics occur as layers of various thickness interbedded with
111 carbonates, indicating repeated explosive eruptions. Analyses of fine-grained, but
112 possibly altered, lapilli suggest that the magmas were tholeiitic to alkali picrites
113 (Griffin et al., 2016). The pyroclastic rocks carry mantle xenoliths (peridotites,
114 pyroxenites) derived from <90 km depth (maximum P-T estimates of ca 1030 °C and
115 2.3 GPa), suggesting a thin lithosphere and a high thermal gradient (Esperanca and
116 Garfunkel, 1986; Mittlefehldt, 1986; Kaminchik et al., 2014; Apter, 2015). They also
117 contain a wide variety of xenocrysts: debris from garnet/spinel peridotites and
118 pyroxenites, and megacrysts of clinopyroxene, ilmenite, zircon and corundum.

119 Aggregates of hopper-formed corundum crystals (Carmel Sapphire™) are
120 common in the pyroclastic ejecta of the volcanoes exposed on Mt Carmel, and in
121 associated alluvial deposits. Melt pockets trapped within and between the skeletal
122 corundum crystals contain mineral assemblages including moissanite (SiC), Fe-Ti-Zr
123 silicides/ phosphides, Ti nitrides and borides, and native V, that require high T
124 (≥ 1450 to ca 1200 °C) and fO_2 from 6 to 9 log units more reducing than the Iron-
125 Wustite buffer ($\Delta IW = -6$ to -9).

126 Paragenetic studies (Griffin et al., 2016, 2018; Xiong et al., 2017; Fig. 1)
127 suggest that the crystallization of corundum and the low fO_2 reflect the interaction of
128 basaltic magmas with mantle-derived CH_4+H_2 at high fluid/melt ratios, leading to
129 progressive reduction and desilication of the magma, and ultimately to Al_2O_3 -
130 supersaturation, the rapid growth of skeletal/hopper corundum crystals, and the
131 deposition of abundant amorphous carbon. This evolution included several stages of
132 liquid-liquid immiscibility, including the segregation of Fe- and Ti-silicide melts from

MS 66733R revised 28-09-2018

133 silicate melts, driven by a progressive decrease in fO_2 . The latest stage of this
134 evolution is defined by the appearance of hibonite, grossite and spinel, suggesting
135 that silica-deficient melts evolved beneath some of the volcanic centers.

136

137 **Methods**

138 The samples, collected and provided by Shefa Yamim, have been mounted in
139 epoxy discs, polished and characterized by optical microscopy, and by back-
140 scattered electron and cathodoluminescence imaging in the scanning electron
141 microscope, to identify minerals and to establish parageneses. Mineral compositions
142 were analysed by both SEM-EDS and WDS electron microprobe. Trace elements
143 were analysed by LA-ICPMS. Selected samples were examined by TEM using FIB
144 foils, and TEM-EDS and TEM-XRD were used to obtain chemical analyses and
145 crystallographic parameters of specific phases. 3D- μ CT scans of individual grains
146 and aggregates were taken to examine structures in three dimensions. Details of
147 each of these methods are given in the Supplementary Data.

148

149 **Petrography**

150 Hibonite from the primary pyroclastic deposits and in placer samples from the
151 Kishon and Yoqneam Rivers occurs in two parageneses. Paragenesis A comprises
152 inclusions in and between skeletal corundum crystals, and paragenesis B the
153 granular aggregates of hibonite+grossite+spinel.

154

155 **Paragenesis A: hibonite in corundum**

156 Hibonite occurs in pockets of trapped melt interstitial to, or included in,
157 corundum crystals within the corundum aggregates (Figs 2, 3). The melt pockets in
158 the corundum aggregates have been described by Griffin et al. (2016; 2018) and
159 Xiong et al. (2017). The earliest parageneses consist of tistarite (Ti_2O_3) \pm a Ti-Al-Zr
160 oxide (informal name: TAZ) \pm Mg-Al spinel in a matrix of Ca-Mg-Al-Si-O glass. The
161 earliest trapped melts represent considerable modification of assumed primary
162 silicate melts (probably basaltic), including progressive desilication by the exsolution
163 of immiscible Fe-Ti oxide melts and Fe-Ti-Zr-silicide melts, and the crystallization of
164 moissanite and khamrabaevite (TiC), at $fO_2 = \Delta IW-6$ or less. This process continued,
165 producing progressively lower fO_2 , witnessed especially by the appearance of Ti^{2+} -

MS 66733R revised 28-09-2018

166 bearing phases (TiB₂, TiN, TiC, TiO). The earliest appearance of hibonite in the melt
167 pockets is in association with TAZ, spinel, TiN, Fe-Ti silicides, TiC and glass,
168 interstitial to corundum crystals (Fig. 2). This hibonite is locally associated with
169 grossite, but appears also to be in textural equilibrium with corundum. In some
170 pockets hibonite is intergrown with or crosscut by at least two unknown Zr-Ti oxides.
171 (Table 1; Fig. 3). These phases and others (Table 1) appear to reflect the
172 continuous concentration of incompatible elements in the silicate melts (percent
173 levels of Ti, Zr, La, Ce; Table 2) as the trapped melt volumes were progressively
174 reduced by the growth of corundum, in parallel with the decrease in fO_2 .

175

176 **Paragenesis B: hibonite-grossite aggregates**

177 Rounded to angular grains ranging from millimeters up to 2.5 cm across
178 consist of flattened hexagonal prisms ($a:c = 7-17$) of hibonite in a matrix of grossite
179 and Mg-Al spinel (Fig. 4). The rough material typically is purplish in colour (Fig. 4a),
180 but in polished, more transparent grains some has a yellow-orange colour. The
181 hibonite displays orange cathodoluminescence, while that of grossite is blue to
182 purple. A characteristic feature is the occurrence of balls and dendrites of native
183 vanadium, included in hibonite and grossite, and more rarely in spinel.

184 The major paragenesis of these intergrowths is shown in Figures 5-7.
185 Hibonite occurs as tabular crystals up to 1 cm across, in a matrix of granular grossite
186 and spinel (commonly as euhedral octahedra); fluorite is the last phase to crystallize.
187 Resorbed remnants of corundum in some hibonite laths (Figs 5,6) indicate that
188 corundum crystallized before the Ca-Al-oxides and that hibonite crystallized via the
189 peritectic reaction corundum (Cor) + liquid/melt (L) → hibonite. This was followed by
190 the cotectic precipitation of grossite, hibonite and spinel, and finally the assemblage
191 grossite + spinel + CaAl₂O₄ (krotite) + fluorite.

192 Grossite commonly is euhedral against interstitial fluorite. The oxyfluoride
193 phase Ca₄Al₆F₂O₁₂ (widely synthesised, but not previously reported in nature)
194 appears to precede fluorite in the crystallization sequence and to coexist with
195 grossite. Rare grains of perovskite (CaTiO₃) also appear to coexist with grossite (Fig.
196 5c; Table 1) or intergrown with fluorite (Fig. 5d).

197 Most of the hibonite-grossite aggregates show little or no preferred orientation
198 of the hibonite crystals, but some have radiating structures. In the example shown in
199 Figure SD2, the hibonite + grossite + spinel + fluorite assemblage appears to have

MS 66733R revised 28-09-2018

200 grown from a substrate of coarse-grained grossite; the width of the hibonite tablets
201 increases with distance from the contact, suggesting a quench-related structure.

202 Small drop-like grains of native vanadium (V^0) are common in hibonite and
203 grossite (Fig. 5a,b), indicating the lowering of fO_2 to $\Delta IW \leq -9$, where V^0 becomes
204 stable (Fig. 1). It occurred roughly at the temperature of the peritectic reaction cor + L
205 = hibonite, although there is no obvious reason for the two reactions to be linked.
206 Native V also occurs as balls up to 500 μm across, either isolated within hibonite, or
207 together with grossite and fluorite in complex pockets among hibonite grains (Fig.
208 8a). These larger balls contain percent levels of Cr and Mn, and have exsolved into
209 laths of V^0 with higher and lower levels of these two elements (Fig. 8b,c; Table 1).
210 Some of these balls are altered to mixtures of fluorite and carbonates (Fig. 8d)
211 related to cracks, some of which are filled with an Al-hydroxide, possibly gibbsite.
212 Larger cracks contain pockets with a geode-like zoned filling of this phase, including
213 terminated crystals extending into open voids. Since the assemblage $V^0 + \text{CaF}_2$
214 apparently is stable in other situations (Fig. 8a), this alteration is interpreted as a
215 post-eruption phenomenon.

216 In some cases, vanadium in hibonite develops from drop-like balls with worm-
217 like protuberances (Fig. 8), into spectacular 3D dendritic growths (Fig. 9; Fig. SD3),
218 growing sub-parallel to the c axis of the hibonite crystals.

219

220 Mineral chemistry

221 Major and minor elements

222 Hibonite included in corundum (paragenesis A) contains significant levels of
223 Si, Zr, Ti, Cr, Sr, Mg and LREE (up to >6% Ce_2O_3 ; Table 1), but does not contain
224 measurable levels of V. TEM imaging shows a hexagonal cell with $c = 22.73 \text{ \AA}$,
225 compared to 22.29 Å in the type material; the a axis is 4.8 Å , shorter than in the type
226 material (5.6 Å). Calculation of the structural formula on the basis of 19 oxygens
227 indicates that essentially all of the Ti is present as Ti^{3+} . The apparent deficit in
228 trivalent ions in the formula (Table 1) probably reflects the levels of other REE (see
229 below) that are below the detection limit of the EMP (ca 0.1 wt%). In contrast,
230 hibonite in the granular aggregates (paragenesis B) contains percent levels of V, and
231 minor levels of Mg, but all other elements are below detection for the EMP.

MS 66733R revised 28-09-2018

232 Calculation of the structural formula (Table 1) suggests that V is present as V^{3+} , or
233 even partly as V^{2+} .

234 Grossite is essentially stoichiometric $CaAl_4O_7$ with no minor elements at the
235 EMP level. The Raman spectrum of the stoichiometric phase $CaAl_2O_4$ (Table 1)
236 identifies it as the low-pressure form krotite, rather than the high-pressure form
237 dimitryivanovite. This is consistent with available pressure constraints (see below)
238 that suggest crystallization at around 1 GPa, while dimitryivanovite is stable above 2
239 GPa (Mikouchi et al., 2011). To our knowledge, this is the first natural terrestrial
240 occurrence of krotite, originally described from a CAI in a CV3 carbonaceous
241 chondrite (Ma et al., 2011).

242 Spinels occurring in melt pockets with hibonite (paragenesis A) are essentially pure
243 Mg-Al spinels, with a deficit in Mg and an excess of Al. This feature is common to
244 spinels in the less-evolved melt pockets without hibonite (our unpublished data),
245 suggesting that either Ti or Al substitutes for Mg, but it is not clear from the analyses
246 how charge balance would be achieved. Spinels in the hibonite-grossite aggregates
247 (paragenesis B) show a range of compositions, related to the presence of native V.
248 Spinels in aggregates with no visible V^0 contain 9-16 wt% V (4.5-8 at%), and 1.7-8%
249 wt% Mn; with a few exceptions, the contents of V and Mn are positively correlated,
250 while both MgO and Al_2O_3 show negative correlations with V_2O_3 (Figure SD4).
251 Detailed studies of the related phase dellagiustaitite (ideally AlV_2O_4 ; Camara et al.,
252 2018), show all vanadium is ordered in the octahedral sites, with Al in the tetrahedral
253 site; $^AAl^B(V^{2+}V^{3+})O_4$ (where A are tetrahedral sites and B are octahedral sites). It
254 seems likely that this is also the case in the high-V spinels reported here.

255 Spinels in aggregates with scattered small beads of V^0 contain 2-5 wt% V and
256 0.3-1.3 wt% Mn. In aggregates with abundant V^0 , the spinels mostly contain <0.5
257 wt% V and Mn. These less V-rich spinels have 2.0 Al ions per formula unit,
258 suggesting that all of the V substitutes for Mg.

259 The Ca-Al oxyfluoride in the hibonite-grossite-spinel aggregates (Figs 5, 6)
260 has the formula $Ca_4Al_6O_{12}F_2$; it is known from experimental studies on the CaO-
261 Al_2O_3 -F system (Kim, 2011). F. Cámara, R. Pagano, A. Pagano, L. Bindi and F.
262 Nestola have described this phase in similar material from Sierra de
263 Comechingones, San Luis, Argentina, and have proposed the name calfidine (IMF
264 proposal number 2018-093; not yet approved).

MS 66733R revised 28-09-2018

265 All EDS analyses of fluorite contain carbon, and may fit a formula $\text{CaF}_{2-x}\text{C}_x$.
266 The EMP analyses did not include carbon, but the deficiency in the sums suggests
267 the presence of a missing component such as carbon.

268 The perovskite phase has the formula CaTiO_3 , implying that the Ti is present
269 as Ti^{4+} ; this is anomalous at the $f\text{O}_2$ implied by its coexistence with V^0 . It also contains
270 1.6 wt% V and 1.3 wt% F.

271 The only Zr-Ti oxide grain large enough to analyse by EMP (Fig. 3) contains
272 minor amounts of Al, Mn, Mg and Ca; the structural formula of the mean analysis
273 (Table 1) can be simplified as Zr_3TiO_8 , implying that Ti is present as Ti^{4+} . However,
274 the large standard deviations on the mean analysis indicate that this “phase” is very
275 heterogeneous. Multiple SEM-EDS analyses which sample smaller volumes (Table
276 1) suggest the presence of several other oxides with variable ratios of $(\text{Zr}+\text{Ti})/\text{O}$, in
277 which Ti appears to be present as Ti^{3+} . These may represent breakdown products of
278 the Zr_3TiO_8 phase shown in Figure 3, but most occur as discrete grains. Further
279 TEM studies will be required to confirm the nature of these phases.

280 The smallest vanadium spheres are nearly pure V^0 , with 0.5-2 wt% Si and 1.5-
281 2.5 wt% Mn. As these are inclusions in hibonite or corundum, the Si is assumed
282 to substitute in the alloy, rather than being a matrix contamination. Most larger V
283 inclusions have lower Si, but contain 1-2% Cr and 0.5-3.5% Mn, and may have up to
284 ca 4 wt% Al (V_9Al ; Table 1; Figure 9). The latest to form are irregular balls with drop-
285 like protruberances, that occur in nests of grossite surrounded by laths of hibonite
286 (Fig. 8). These are similar in form to the drops that develop into the spectacular
287 dendrites (Figs 9, SD3). They contain even higher levels of Al, with up to 15 wt%
288 and a mean of 12% (V_4Al ; Table 1); single-crystal XRD has confirmed a cubic
289 structure (L. Bindi, pers. comm., August 2018).

290

291 **Trace elements**

292 Mean trace-element data for the major phases, from LA-ICPMS analysis, are
293 given in Table 3 and shown in Figure 10.

294 Hibonite in the corundum aggregates (paragenesis A) is extremely enriched in
295 the REE ($\Sigma\text{REE} = 2.7$ wt%) with a moderate enrichment in LREE over HREE. It
296 shows small negative anomalies in Sr, Eu and Y, and a positive anomaly in Yb. Ti
297 reaches 1.7 wt%, Sr 1 wt% and Zr 0.35 wt%. Th + U are also enriched (0.3 and 0.04

MS 66733R revised 28-09-2018

298 wt%), while vanadium is very low (2 ppm). CHECK against Table, which shows
299 higher values? Fe is absent, although minor Mn (34 ppm) is present; the only other
300 transition element is Ni (3.5 ppm).

301 Hibanite in the hibanite-grossite aggregates (paragenesis B) shows LREE
302 enrichment, and a mild depletion in HREE relative to chondrites; Ba is depleted
303 relative to Ce and La. The extended REE pattern is essentially parallel to that of the
304 mean hibanite in paragenesis A (Fig. 10b), but lower in most elements by ca two
305 orders of magnitude, and shows a relative depletion in Zr. One grain (982-2c-01)
306 shows an unusual depletion in the lighter elements (Sr to Ce, Ba) while the other
307 REE levels are similar to those in the mean hibanite. Most grains show negative Eu
308 anomalies ($\text{Eu}/\text{Eu}^* = 0.2\text{-}0.82$, mean 0.46, $n=9$), but the other anomalies seen in the
309 interstitial-hibanite pattern are absent. Ti contents in the hibanites of paragenesis B
310 range from 70-720 ppm, and are roughly correlated with V contents, which range
311 from 1100-13300 ppm. The highest V contents are found in grains with small
312 inclusions of V^0 , although care was taken to avoid these during analysis. The next
313 most abundant transition element is Mn (50-580 ppm) and most grains carry low
314 levels of Fe and/or Cr. Th and U contents are scattered (1-17 ppm and 1.4-4 ppm,
315 respectively) but Th/U ratios show less spread ($3.8 \pm 2.1(1\sigma)$). Most Na values are
316 around 20 ppm, but K is <0.02 wt% in most grains. B is reported at levels of 20-50
317 ppm (but is <2 ppm in one); we cannot be confident of these values, but note that the
318 Mt Carmel system does contain boride minerals (TiB_2 ; Griffin et al., 2016).

319 Grossite in paragenesis B has generally chondritic to subchondritic levels of
320 the REE, and low levels of most other trace elements (Fig. 10c). The high standard
321 deviations relative to the absolute values suggest that many of these elements reside
322 in tiny inclusions of other minerals, or melt, inside the grossite. Most grains show a
323 pattern with relatively flat HREE and MREE, and depleted LREE; the patterns and
324 absolute abundances of Y and the HREE are similar to those of coexisting hibanite
325 (Fig. 10b,c). However, some grains do not show the LREE depletion. Ba is elevated
326 relative to La and Ce, and all grains show high levels of Sr and Y compared to the
327 MREE, although the absolute levels are similar to those in hibanite. In contrast to
328 the hibanite, most grains of grossite show a small positive Eu anomaly. Ti (30-120
329 ppm) contents are lower than in hibanite, but contents of V (850-2750 ppm) and Mn
330 (0-510 ppm) overlap the ranges seen in hibanite, and Fe levels (mostly 100-250

MS 66733R revised 28-09-2018

331 ppm) are higher. There is no obvious correlation between Ti and V. In marked
332 contrast to the hibonites, contents of Th and U in grossite are typically <0.05 ppm.

333 *Large spinel* grains in paragenesis B contain ca 2.5% V; Mn contents range
334 from 3100-6400 ppm, while Cr, Ti and Zn values average 77, 150 and 10 ppm,
335 respectively. Ga contents are < 0.2 ppm, giving very high Al/Ga ratios. Ca contents
336 are unusually high for spinels, at 1100-4300 ppm.

337 A single LA-ICPMS analysis of a large *vanadium* sphere in hibonite gave
338 values of 490 ppm Zn, 21 ppm Cu, and 69 ppm Nb.

339

340 **DISCUSSION**

341 ***Conditions of formation***

342 *Temperature*

343 The temperatures during the crystallization of the Mt Carmel super-reduced
344 assemblages can be estimated from experimental data, which are mainly from 1-atm
345 experiments. Therefore the estimated temperatures may represent minimum values
346 in the individual simple systems. The major phases all lie within the simple and well-
347 studied system CaO-MgO-Al₂O₃-SiO₂; the coexisting melts consist mainly of these
348 oxides, though with significant levels of Ti, Zr and REE.

349 Hibonite crystallizes from CaO-Al₂O₃ melts (Fig. 11a) via the peritectic
350 reaction Crn + Liq → hibonite; different experimental or theoretical studies place this
351 reaction at 1850-1880 °C; in more SiO₂-rich systems (Fig. 12) the peritectic extends
352 down to ca 1475 °C. There is disagreement in the literature as to the nature of
353 lower-temperature phase transitions on this binary. Some studies (e.g. Guo et al.,
354 2015; Azof et al., 2017) show both grossite and krotite melting congruently,
355 producing the binary eutectics Hbn + Gros + Liq and Gros + Krot + Liq. Others (e.g.
356 Mao et al 2004) show both phases melting incongruently, in peritectic reactions Hbn
357 → Gros + Liq and Gros → Krot + Liq. Still others show singularities in which the
358 peritectic reactions correspond to the congruent melting points of grossite and
359 krotite, respectively. The older experimental work is more consistent with the
360 modeling of Mao et al. (2004; Fig. 12). In the aggregates of Paragenesis B, there is
361 no obvious reaction relationship between hibonite and grossite, but the grossite
362 +spinel assemblage does appear to crystallize after hibonite.

363 Grossite (Gros) appears at 1750-1780 °C in the binary system, and krotite at
364 ca 1600 °C. In the 1-atm. CaO-MgO-Al₂O₃ system (Fig. 11c) the Hbn+Gros+Liq

MS 66733R revised 28-09-2018

365 peritectic descends to the Gros+Spl+Liq cotectic at ca 1690 °C. In the 1-atm.
366 liquidus diagram two intermediate Ca-Al-Mg oxides appear through peritectic
367 reactions just above this temperature (Fig. 11b), but these phases have not been
368 recognised in the Mt Carmel system. Their apparent absence may be a pressure
369 effect (see below), or it may reflect the presence of abundant fluorine in the system,
370 effectively sequestering Ca. Alternatively, they may have been consumed in
371 peritectic reactions. The presence of krotite as an interstitial late phase implies that
372 the residual melts evolved further, toward the peritectic Gros + Liq (\pm spinel) \rightarrow krotite
373 at ca 1520 °C (Fig. 11b). Krotite + Spn + Liq coexist along a cotectic leading to more
374 Ca-rich compositions, not seen in our samples, at ca 1350 °C

375 The presence of fluorine may lower these liquidus temperatures. The fluorite-
376 grossite assemblage precipitates at ca 1375 °C in the 1-atm. CaF_2 - CaAl_2O_4 system
377 and the $\text{Ca}_4\text{Al}_6\text{O}_{12}\text{F}_2$ phase crystallizes from ca 1480 °C to a eutectic with fluorite at
378 1375 °C (Fig. SD5; Kim, 2011). $\text{Ca}_4\text{Al}_6\text{O}_{12}\text{F}_2$ is unstable at $T < 1150$ °C, providing a
379 lower limit for the cooling of the system before eruption terminated the evolution of
380 the melts. The presence of this phase implies that F^{1-} had replaced a significant
381 amount of the O^{2-} in the melt (Peng et al., 2011).

382 One spinel has been found coexisting with hibonite in the melt pockets (Table
383 1). Like spinels coexisting with tistarite and the TAZ phase in the earlier stages of
384 the melt evolution, it has a large excess of Al_2O_3 and a deficit in divalent cations; by
385 comparison with the experimental MgO - Al_2O_3 system (e.g. Bhaduri and Bhaduri,
386 1999; Callister, 2008) it gives a T close to 1400 °C, within the range of temperatures
387 derived from spinels in other melt pockets (1600 °C to 1200 °C, with a mean of 1400
388 °C; our unpublished data). In contrast, the spinels in the hibonite-grossite
389 aggregates are nearly stoichiometric $(\text{Mg}, \text{V})\text{Al}_2\text{O}_4$, which yields a temperature
390 around 1200 °C.

391

392 *Pressure:* There are no independent constraints on the pressure of formation for the
393 hibonite-grossite assemblage; it crystallized at very low pressure in the Solar nebula
394 (Beckett et al., 2006), at ca 1-2 km depth in the Hatrurim Formation (Gross, 1977),
395 and at ca 10-30 km depths in the granulite-facies occurrences (Rakotondrazafy et
396 al., 1996). Dmisteinbergite, the metastable high- T hexagonal polymorph of anorthite,
397 occurs as a quench phase in many melt pockets (Xiong et al., 2017). In
398 experiments, this phase can be produced by rapid cooling of the melt to ca 1200 °C

MS 66733R revised 28-09-2018

399 (Davis and Tuttle, 1952). In the present case, this reflects the peritectic reaction Crn
400 + Liq → An, which is constrained experimentally to $P_{\min} > 0.9$ GPa and $T \text{ ca } 1450$ °C
401 (Goldsmith, 1980). The parageneses in the hibonite-grossite aggregates (Figs 5, 6)
402 document crystallization across the peritectic $\text{Liq} + \text{Crn} \rightarrow \text{hibonite}$, followed by
403 crystallization along the hibonite-grossite cotectic to where it joins the cotectic Gros
404 + Spl + Liq. Ottonello et al. (2013) modelled the CaO-Al₂O₃-SiO₂ liquidus at
405 pressures to 2 GPa, and argued that grossite is not a liquidus phase at $P \geq 1$ GPa
406 (Fig. 13). The presence of CaAl₂O₄ as krotite, rather than the higher-P polymorph
407 dmitryivanovite, also limits P to < 2 GPa (Mikouchi et al., 2009). If these constraints
408 are accepted, the Mt Carmel corundum-SiC system was crystallizing at $P = \text{ca } 1$ GPa
409 (depths of 25-30 km) near the crust-mantle boundary in the area (Segev and
410 Ryabkov, 2011), when the host basalts erupted.

411

412 *Oxygen fugacity (f_{O_2}):* Hibonite is stable over a wide range of oxygen fugacity. The
413 Mt Carmel assemblages described here require very reducing conditions, consistent
414 with the occurrence of tistarite (Ti₂O₃) and SiC as inclusions in corundum. The
415 presence of a positive Yb anomaly in the hibonite of paragenesis A is consistent with
416 this low f_{O_2} , as Yb²⁺ will substitute for Ca in the hibonite more readily than Yb³⁺. In
417 the hibonite-grossite aggregates of paragenesis B, the coexistence of native V
418 requires $f_{\text{O}_2} < \Delta\text{IW}-8$ (Fig. 1). As noted above, low oxygen fugacity is not a pre-
419 requisite for the crystallization of the hibonite-grossite-spinel assemblage. However,
420 it was the progressive lowering of f_{O_2} during the evolution of the magmatic system
421 that led to the immiscibility of silicide melts, driving the desilication of the magma that
422 ultimately allowed the crystallization of the oxide assemblage hibonite-grossite-spinel
423 (Griffin et al., 2016; Xiong et al., 2017).

424 In summary, the crystallization of the hibonite-grossite assemblage in the Mt
425 Carmel system probably occurred at depths of 25-30 km, temperatures falling from
426 ca 1500 °C to ca 1200 °C prior to eruption, and f_{O_2} between $\Delta\text{IW} -6$ and $\Delta\text{IW} -9$.

427

428 **Melt Evolution**

429 For a rough estimate of the composition of the bulk crystallization products,
430 element maps of eight hibonite-grossite aggregates were point-counted to determine
431 the modal abundances of the analysed phases, and bulk compositions were

MS 66733R revised 28-09-2018

432 calculated. These proved to show little variation in composition (Table 2); the mean
433 contains ca 80 wt% Al₂O₃, 16 wt% CaO, 2 wt% MgO and 1 wt% F, while other
434 components are present at levels of ≤0.5%. This composition lies close to the
435 hibonite-grossite boundary on the CA binary (Fig. 11a), and the CAS ternary plot
436 (Fig. 12), but in the field of corundum in the CMA ternary (Fig. 11b).

437 The major-element composition of a melt coexisting with the average hibonite
438 in paragenesis A (24 analyses) was calculated using the D values of Kennedy et al.
439 (1994), based on 1-atm. experimental studies, and our own values derived from a
440 single hibonite-glass pair (Fig. 2). There are obvious hurdles in this approach, in
441 terms of concentration levels and non-ideality of melts, but the data may be useful on
442 a comparative basis. The value for $D_{\text{Si}}^{\text{h/m}}$ given by Kennedy et al. (1994) is clearly
443 not applicable to the Mt Carmel material, as it would predict >100 wt% SiO₂ in the
444 melt. A value for $D_{\text{Si}}^{\text{h/m}}$ derived from our analysis of the glass coexisting with one
445 hibonite in corundum would predict 28 wt% SiO₂ in the melt coexisting with the mean
446 interstitial hibonite. The actual analysed melt contains 38.3 wt% SiO₂, while the
447 interstitial hibonite coexisting with it has higher SiO₂ than the mean value.

448 As expected, the melt predicted using both approaches is very high in Al₂O₃
449 and CaO (Table 3). MgO contents predicted by the data of Kennedy et al. (1994) are
450 higher than our calculated values. The levels of Zr and Ti predicted by both sets of
451 distribution coefficients are similar. This composition lies near the corundum-
452 anorthite cotectic on the CaO-Al₂O₃-SiO₂ (CAS) liquidus phase diagram at 1 atm
453 pressure (Fig. 12), but close to the corundum-hibonite peritectic at 1 GPa (Fig. 13;
454 Ottonello et al., 2013). Glasses coexisting with hibonite in meteoritic spherules,
455 interpreted as melts condensed from the solar nebula (Ireland et al., 1991) are
456 broadly similar in being essentially CMAS melts, but have lower Al and higher Si, Ca
457 and Mg than those calculated for the interstitial hibonite.

458 The calculated major-element composition of the melt in equilibrium with the
459 mean hibonite composition of paragenesis B (Table 3) suggests a further evolution to
460 higher CaO/Al₂O₃, but lower MgO. SiO₂ and TiO₂ are below detection limits in the
461 hibonite, and this may suggest SiO₂ contents ≤20 wt% and TiO₂ contents ≤0.5 wt%
462 in the melt. This composition, though poorly constrained, lies within the CAS liquidus
463 field of corundum at one atm. and at 1 GPa (Figs 12, 13).

464 If the melts calculated for the two parageneses are linked by the evolution of
465 the trapped melts beyond the corundum-hibonite peritectic, that evolution is unlikely

MS 66733R revised 28-09-2018

466 to have been driven only by fractional crystallization of the observed assemblages,
467 which would increase SiO₂ but decrease Al₂O₃ in the melt. However, such an
468 evolution would be broadly consistent with the overall trend seen in the Mt Carmel
469 system, of continued desilication of the silicate melts by immiscible separation of
470 silicide melts and crystallization of SiC, with falling fO_2 (Fig. 13)

471 The Fe-Ti silicide melts that separated from the parental melts earlier in their
472 evolution contain <0.5 wt% V (our unpublished data), suggesting that V did not
473 partition strongly into the metallic melts. This is consistent with the generally
474 lithophile nature of V, and the observation that the partition coefficient
475 $D_V^{\text{metallic melt/silicate melt}}$ decreases (i.e. V becomes more lithophile) with increasing Si
476 content in the metallic melt (Tuff et al., 2011). However, $D_V^{\text{metallic melt/silicate melt}}$ should
477 be higher at low fO_2 ; this may indicate that most of the separation of silicide melts
478 occurred at high enough fO_2 (ΔIW -6 to -7) to hinder a stronger uptake of V, leaving
479 enhanced levels of V in the residual melts.

480 During the further evolution of the melts, there were few crystallizing phases
481 that accepted significant levels of V, until the appearance of the hibonite-related
482 spinels described here. At that point, fO_2 may have been low enough for the stability
483 of both V³⁺ and V²⁺, allowing substitution for Mg and Al in the first spinels, up to 8
484 at.% (Table 1). XANES analysis of V in fassaitic pyroxenes from refractory CAIs has
485 found V²⁺/V^{tot} ratios as high as 0.7, consistent with a solar gas (i.e. H-dominated;
486 Simon et al., 2007). The presence of Ti²⁺-bearing phases (e.g. TiC) and V⁰ suggest
487 that the minimum fO_2 during the late stages of the Mt Carmel system was at least
488 this low (Fig. 1), and thus that H₂ may have been the main volatile species present.

489 Righter et al. (2006; see also Papike et al., 2013) studied the partitioning of V
490 between silicate melts and Al-spinels over a wide range of oxygen fugacity and
491 composition. Using their equation (2) and the constants they calculated from the
492 low- fO_2 experiments, we estimate $D_V^{\text{spinel/silicate melt}}$ to be in the range of 43-45 for the
493 spinels in the hibonite-grossite aggregates. This approach suggests that the melt
494 coexisting with the high-V spinels (Table 1) contained on the order of 1000-1500
495 ppm V. The concentration of V in the late Ca-Al-Si-O melts thus represents only a
496 moderate (5x) enrichment relative to a proposed mafic parental melt (200-300 ppm;
497 Fig. 2). The melt that crystallized the medium-V spinels contained about 400 ppm V,
498 and the melt with the low-V spinels, which crystallized in the presence of V⁰,

MS 66733R revised 28-09-2018

499 contained only about 35 ppm V. This trend partly reflects the rapid sequestration of
500 V into its own melt phase, which is clearly immiscible with the silicate melt.

501

502 **Composition of coexisting melts – Trace Elements**

503 The $D^{\text{hibonite/melt}}$ values for a range of trace-elements published by Kennedy et
504 al. (1994; K94 below), Ireland et al. (1991; I91 below) and Drake and Boynton (1988;
505 DB88 below) allow calculation of the trace-element patterns of the melts that would
506 have equilibrated with the analysed hibonites (Fig. 14a; Table 3). The melts
507 calculated from the interstitial hibonites in the corundum aggregates (paragenesis
508 A) have relatively flat HREE-MREE and mild enrichment in the LREE. The LREE
509 patterns calculated with I91 have lower MREE-HREE than those calculated from the
510 K94 data. The D_{Eu} value of K94 is >1 and produces a negative Eu anomaly, whereas
511 those of I91 and DB88 produce positive Eu anomalies. The three sets of D_{Yb} values
512 all produce a marked positive Yb anomaly in the melts with the interstitial hibonite of
513 paragenesis A. The calculated melts have much higher contents of the REE and
514 other trace elements than melts coexisting with hibonite in meteoritic glass spherules
515 (Ireland et al., 1991; Fig. 14c). However, the meteoritic glasses do not show LREE
516 enrichment, nor any Yb anomaly.

517 The calculated melts in equilibrium with the hibonite of paragenesis B are, as
518 might be expected, much more depleted in most trace elements (except Th, U and
519 Ba), in general rougher (a function of low count rates) and more spoon-shaped than
520 the pattern of the paragenesis-A melt. The melts calculated from the hibonite of
521 paragenesis B have REE levels similar to those of meteoritic glasses, but the
522 patterns are more spoon-shaped than those of the meteoritic glasses.

523 LA-ICPMS analyses of glasses in the melt pockets in the corundum
524 aggregates define three prominent populations, ranging from a high-Ce, low-Ba type
525 to a lower-Ce, higher-Ba type (Fig. 14b; Table 3); all three types have strongly
526 negative Sr anomalies. While the high-Ce glasses have flat HREE-MREE and
527 LREE-enrichment, the lower-Ce glasses have a more concave-upwards pattern. The
528 higher-Ce, lower-Ba glasses are broadly similar to the calculated melt in equilibrium
529 with the interstitial hibonites (paragenesis A). In the pyroclastic ejecta, many
530 fragments of the corundum aggregates are coated in the low-Ce, high-Ba glass,
531 which has patterns even more upward-concave than those of the higher-Ce glasses

MS 66733R revised 28-09-2018

532 (Fig. 14b). These glasses are broadly similar to the calculated melt in equilibrium
533 with the mean hibonite of paragenesis B, but also show many differences.

534 For comparison with the partitioning data of Kennedy et al. (1994), Ireland et
535 al. (1991) and Drake and Boynton (1988), we have calculated the distribution
536 coefficients between the interstitial hibonites (paragenesis A) and the high-Ce, low-
537 Ba glass, and between the aggregate hibonites (paragenesis B) and the low-REE,
538 high-Ba glasses (Table 3). The D values calculated from the interstitial hibonite vs
539 the high-Ce glasses in general agree within a factor of 2 with those of I91 and DB88.
540 Notable exceptions are D_{Sr} , D_V , D_{Zr} and D_{Ba} ; for the latter two the K94 D values look
541 more appropriate. The D values proposed here may be useful in further studies of
542 meteoritic hibonite associations, especially for elements where no D values are
543 otherwise available. The D values calculated by pairing the hibonite of paragenesis
544 B with the high-Ba glass do not provide a good match with any of the other datasets,
545 suggesting that the high-Ba glass, although apparently formed late in the magmatic
546 evolution, was not in equilibrium with the hibonite-grossite-spinel aggregates.

547

548 SUMMARY

549 1. The assemblage hibonite+grossite+spinel of paragenesis A crystallized from
550 evolved, FeO-free, highly-reduced silicate melts trapped within aggregates of
551 hopper/skeletal corundum, found as ejecta in the late Cretaceous mafic-ultramafic
552 explosive-pyroclastic volcanic rocks exposed on Mt Carmel, N. Israel. Coexisting
553 minerals indicate $fO_2 \leq \Delta IW -6$. These highly reducing conditions are attributed to
554 interaction between mantle-derived CH_4+H_2 fluids and mafic magmas near the base
555 of the crust (25-30 km).

556

557 2. Coarse-grained aggregates of hibonite + grossite + spinel + fluorite \pm krotite \pm
558 perovskite \pm $Ca_4Al_6O_{12}F_2$ (paragenesis B) appear to represent the further evolution of
559 the silicate melts. Textural evidence shows that hibonite crystallized via the
560 peritectic reaction $Crn + Liq \rightarrow Hbn$, and was succeeded by $Hbn + Gros + Spl$.

561

562 3. Native vanadium occurs as rounded inclusions in the hibonite, grossite and spinel
563 of the coarse aggregates; some of these inclusions develop into spectacular
564 dendritic clusters roughly parallel to the c axis of hibonite crystals. The presence of

MS 66733R revised 28-09-2018

565 V^0 requires $fO_2 \leq \Delta IW -9$, suggesting a decline in fO_2 by ca 3 log units during the
566 crystallization of this assemblage.

567

568 4. Spinels in the hibonite + grossite + spinel aggregates contain 9-15 wt% V; those
569 coexisting with minor V^0 contain 3-5 wt% V, and those coexisting with abundant V^0
570 contain ≤ 0.5 wt% V. In high-V spinels, vanadium appears to be present as both V^{2+}
571 and V^{3+} , while in lower-Al spinels it may be present as V^{2+} ; these spinels are
572 essentially stoichiometric $(Mg,V)Al_2O_4$, and are consistent with crystallization
573 temperatures around 1200°C.

574

575 5. The late crystallization of the previously-unreported phase $Ca_4Al_6O_{12}F_2$ together
576 with fluorite in the hibonite-grossite-spinel aggregates (paragenesis B) suggests that
577 crystallization of the aggregates began at $T > 1400$ °C, cooled to the pseudo-eutectic
578 $Gros + Fl + Ca_4Al_6O_{12}F_2 + Liq$ at ca 1375 °C, and remained at $T > 1150$ °C until
579 crystallization was terminated by the volcanic eruption. This is consistent with the
580 appearance of dmisteinbergite as a quench phase in melt pockets in corundum.

581

582 **IMPLICATIONS**

583 This is the first reported terrestrial example of the crystallization of hibonite and
584 grossite from high-T silicate melts, the first terrestrial occurrence of krotite, and the
585 first report of native vanadium melts. The Mt Carmel assemblages described here
586 are analogous in many ways to those observed in many CAI inclusions in
587 carbonaceous chondrites. The inferred conditions of crystallization of the Mt Carmel
588 assemblages are similar to those of the CAIs in terms of temperature and fO_2 , but
589 appear to have formed at higher pressures, ca 1 GPa. The analogies suggest that
590 the Mt Carmel system also formed in the presence of abundant H_2 and carbon.

591 These unusual mineral assemblages thus reflect a magmatic environment in which
592 fO_2 was reduced to levels that imply coexistence with fluid phases dominated by
593 hydrogen. Such environments have not previously been reported on Earth. Their
594 existence suggests previously unrecognised processes, which may be widespread in
595 connection with deepseated magmatism (Griffin et al., 2018). The observations
596 presented here emphasise the importance of immiscibility between silicate melts and
597 metallic melts under conditions of low fO_2 , and this may be a significant factor in

MS 66733R revised 28-09-2018

598 element fractionation and partial melting in a metal-saturated mantle. The depth(s)
599 of origin of the CH₄-dominated volatile fluxes identified here remains to be
600 determined, but the proposed transfer of such volatiles to shallow depths by deep-
601 seated magmatism implies a deep source, and may represent an underappreciated
602 part of the deep carbon cycle

603

604 **Acknowledgements**

605 We thank Dr. E. Sass and Prof. Oded Navon for useful discussions on the
606 geology of Mt Carmel and the volcanism of Israel in general. The project benefitted
607 greatly from the skill and dedication of the Shefa Yamim operational staff at Akko
608 and especially the mineral sorters. Paul Asimov, David Mittlefelhdtd and handling
609 editor E.B. Watson provided constructive reviews and advice This study used
610 instrumentation funded by ARC LIEF and DEST Systemic Infrastructure Grants,
611 Macquarie University and industry. This is contribution 1209 from the ARC Centre of
612 Excellence for Core to Crust Fluid Systems (www.cafs.mq.edu.au) and 1256 from the
613 GEMOC Key Centre (www.gemoc.mq.edu.au).

614

615 **References**

- 616 Apter, D.B., 2014. High pressure indicator minerals from the Rakefet magmatic complex
617 (RMC), Mt.Carmel, Israel. Abstracts Kimberley Diamond Symposium, Kimberley,
618 South Africa.
- 619 Beckett, J.R., Connolly, H.C., Ebel, D.S. (2006) Chemical processes in igneous Calcium-
620 Aluminum-rich inclusions: A mostly CMAS view of melting and crystallization. *In*
621 Lauretta, D.S., McSween, H.Y. (eds) Meteorites and the Early Solar System II.
622 University of Arizona Press. pp. 389-429.
- 623 Bhaduri, S., Bhaduri, S., 1999. Phase and microstructural evolution of heat treated
624 nanocrystalline powders in Al₂O₃-MgO binary system. *Nanostructured materials*,
625 11(4): 469-476.
- 626 Callister, W.D.J., 2007. *Materials Science and Engineering: An introduction* (7th ed.). John
627 Wiley and Sons, Inc.
- 628 Cámara, F., Pagano, R., Pagano, A., Bindi, L. (2018) Dellagiustaite, IMA 2017- 101. *CNMNC*
629 *Newsletter* No. 42, April 2018, page 446; *Mineralogical Magazine*, 82: 445–451.
- 630 Curien, H., Guillemin, C., Orcel, J., Steinberg, M., 1956. La hibonite, nouvelle espece
631 minerale. *Compte Rendu Academie Scientifique Paris*, 242: 2845–2847 (In French).
- 632 Davis, G.L., Tuttle, O.F., 1952. Two new crystalline phases of the anorthite composition,
633 CaO.Al₂O₃.2SiO₂. *American Journal Science*, Bowen 250A: 107-114.
- 634 Drake, M.J., Boynton, W.V., 1988. Partitioning of Rare Earth Elements Between Hibonite and
635 Melt and Implications for Nebular Condensation of the Rare Earth Elements.
636 *Meteoritics*, 23(1): 75-80.

MS 66733R revised 28-09-2018

- 637 Esperança, S., Garfunkel, Z., 1986. Ultramafic xenoliths from the Mt. Carmel area (Karem
638 Maharal Volcano), Israel. *Lithos*, 19(1): 43-49.
- 639 Gentile, A.L., Foster, W.R., 1963. Calcium hexaluminate and its stability relations in the
640 system CaO-Al₂O₃-SiO₂. *Journal American Ceramics Society*, 46:74-76.
- 641 Goldsmith, J.R., 1980. The melting and breakdown reactions of anorthite at high pressures
642 and temperatures. *American Mineralogist*, 65(3-4): 272-284.
- 643 Griffin, L.W. et al., 2018. Super-reducing conditions in ancient and modern volcanic systems:
644 Sources and behaviour of carbon-rich fluids in the lithospheric mantle. *Mineralogy
645 and Petrology*, <https://doi.org/10.1007/s00710-018-0575-x>.
- 646 Griffin, W. et al., 2016. First terrestrial occurrence of tistarite (Ti₂O₃): Ultra-low oxygen
647 fugacity in the upper mantle beneath Mount Carmel, Israel. *Geology*: G37910.
- 648 Gross, S., 1977. The Mineralogy of the Hatrurim Formation Israel. Geological Survey of Israel,
649 80 pp.
- 650 Grossman, J.N., Rubin, A.E., MacPherson, G.J., 1988. ALH85085: a unique volatile-poor
651 carbonaceous chondrite with possible implications for nebular fractionation
652 processes. *Earth and Planetary Science Letters*, 91(1): 33-54.
- 653 Grossman, L., Beckett, J.R., Fedkin, A.V., Simon, S.B., Ciesla, F.J., 2008. Redox conditions in
654 the solar nebula: Observational, experimental, and theoretical constraints. *Reviews
655 in Mineralogy and Geochemistry*, 68(1): 93-140.
- 656 Guo, C., Shang, S., Du, Z., Jablonski, P.D., Gao, M.C., Liu, Z-K., 2015. Thermodynamic modeling
657 of the CaO-CaF₂-Al₂O₃ system aided by first-principles calculations. *CALPHAD*,
658 48:113-122.
- 659 Ireland, T.R., Fahey, A.J., Zinner, E.K., 1991. Hibonite-bearing microspherules: A new type of
660 refractory inclusions with large isotopic anomalies. *Geochimica et Cosmochimica
661 Acta*, 55(1): 367-379.
- 662 Jerebtsov, D.A., Mikhailov, G.G., 2001. Phase diagram of CaO-Al₂O₃ system. *Ceramica
663 International*, 27,:25-28.
- 664 Kaminchik, J., Segev, A., Katzir, Y., 2014. The origin of intraplate alkaline mafic magmatism in
665 continental shelves: lavas and xenoliths from the Upper Cretaceous volcanos of Mt
666 Carmel. Unpublished MSc thesis, Beer Sheva University, Israel.
- 667 Kennedy, A.K., Lofgren, G.E., Wasserburg, G.J., 1994. Trace-element partition coefficients for
668 perovskite and hibonite in meteorite compositions. *Chemical Geology*, 117(1): 379-
669 390.
- 670 Kim, D.-G., 2011. Experimental Study and Thermodynamic Modelling of the CaO-SiO₂-
671 Al₂O₃-CaF₂ System. Master Thesis, McGill University Libraries.
- 672 Konovalenko, S.I., Ananyev, S.A., Garmayeva, S.S., 2012. Rare and new minerals of the
673 Tashelga-Maizaskaya zone of Gornaya Shoriya, their peculiarities and nature. *Journal
674 of Siberian Federal University—Engineering and Technologies*, 5: 301-310.
- 675 Ma, C. et al., 2011. Krotite, CaAl₂O₄, a new refractory mineral from the NWA 1934
676 meteorite. *American Mineralogist*, 96(5-6): 709-715.
- 677 Mikouchi, T. et al., 2009. Dmitryivanovite: A new high-pressure calcium aluminum oxide
678 from the Northwest Africa 470 CH₃ chondrite characterized using electron
679 backscatter diffraction analysis. *American Mineralogist*, 94(5-6): 746-750.
- 680 Mittlefehldt, D.W., 1986. Petrology of high pressure clinopyroxene series xenoliths, Mount
681 Carmel, Israel. *Contributions to Mineralogy and Petrology*, 94(2): 245-252.
- 682 Osborn, E.F., Muan, A., 1964. In: Levin, E.M., Robbins, C.R., McMurdie, H.F. (Eds.),
683 *Phase Diagrams for Ceramists*. The American Ceramic Society, Columbus, OH.

MS 66733R revised 28-09-2018

- 684 Vol. 1, 219 pp.
- 685 Ottonello, G. et al., 2013. Thermodynamic investigation of the CaO–Al₂O₃–SiO₂ system at
686 high P and T through polymer chemistry and convex-hull techniques. *Chemical*
687 *Geology*, 346: 81-92.
- 688 Papike, J. et al., 2013. Developing vanadium valence state oxybarometers (spinel-melt,
689 olivine-melt, spinel-olivine) and V/(Cr+ Al) partitioning (spinel-melt) for martian
690 olivine-phyric basalts. *American Mineralogist*, 98(11-12): 2193-2196.
- 691 Peng, K.W., Zhang, P., Xie, J.G., Ma, H.L., 2012. Study on Properties of Al₂O₃ -CaO-SiO₂-CaF₂
692 Slag System. *Advanced Materials Research*, 396-398: 786-790.
- 693 Rakotondrazafy, M.A., Moine, B., Cuney, M., 1996. Mode of formation of hibonite
694 (CaAl₁₂O₁₉) within the U-Th skarns from the granulites of S-E Madagascar.
695 *Contributions to Mineralogy and Petrology*, 123(2): 190-201.
- 696 Righter, K., Sutton, S.R., Newville, M., Le, L., Schwandt, C.S., Uchida, H., Lavina, B., Downs,
697 R.T., 2006. An experimental study of the oxidation state of vanadium in spinel and
698 basaltic melt with implications for the origin of planetary basalt. *American*
699 *Mineralogist*, 91: 1643-1656.
- 700 Sass, E., 1980. Late Cretaceous volcanism in Mount Carmel, Israel. *Israel Journal of Earth*
701 *Sciences*, 29(1-2): 8-24.
- 702 Segev, A., Rybakov, M., 2011. History of faulting and magmatism in the Galilee (Israel) and
703 across the Levant continental margin inferred from potential field data. *Journal of*
704 *Geodynamics*, 51(4): 264-284.
- 705 Simon, S.B., Sutton, S.R., Grossman, L., 2007. Valence of titanium and vanadium in pyroxene
706 in refractory inclusion interiors and rims. *Geochimica et Cosmochimica Acta*, 71(12):
707 3098-3118.
- 708 Tuff, J., Wood, B.J., Wade, J., 2011. The effect of Si on metal-silicate partitioning of
709 siderophile elements and implications for the conditions of core formation.
710 *Geochimica et Cosmochimica Acta*, 75: 673-690.
- 711 Xiong, Q. et al., 2017. Super-reduced mineral assemblages in “ophiolitic” chromitites and
712 peridotites: the view from Mount Carmel. *European Journal of Mineralogy*, 29(4): 57-
713 570.
- 714 Yoneda, S., Grossman, L., 1995. Condensation of CaO-MgO-Al₂O₃-SiO₂ liquids from cosmic
715 gases. *Geochimica et Cosmochimica Acta*, 59(16): 3413-3444.

716 **Figure Captions**

718 Figure 1. (a) Schematic evolution of a mafic magmatic system progressively reduced
719 by interaction with mantle-derived CH₄+H₂ fluids. Boxes illustrate the reconstructed
720 sequence of mineral assemblages; the relative variations in major elements through
721 this process are not to scale, but are intended to emphasize the effects of reduction,
722 crystallization and the immiscibility of silicide melts. (b) relative positions of relevant
723 *f*O₂ buffers at 1500 °C, 1 atm. (after Papike et al., 2016).

724

MS 66733R revised 28-09-2018

725 Figure 2. Hibonite in corundum. (a) BSE image of hibonite and associated phases in
726 melt pocket in corundum; (b) closeup BSE image of hibonite; note euhedral
727 terminations on corundum crystals, and residual glass in outermost thin wedge.

728

729 Figure 3. Zr_3TiO_8 “phase” with irregular borders crosscutting hibonite in melt pocket
730 in corundum; note presence of spinel. The Zr_3TiO_8 phase is heterogeneous on a
731 small scale, as reflected in its speckled appearance, and breaks up in contact with
732 Ca-Mg-Al-oxide glass (black), suggesting that both were melts during emplacement
733 of the Zr_3TiO_8 phase.

734

735 Figure 4. Hibonite-grossite aggregates. (a) large grain of hibonite-grossite aggregate
736 with mm-size spheres of native V (V^0); (b) transmitted-light photo of transparent
737 specimen, enclosing black spinel grain and rods of V^0 ; (c) phase map of (b) showing
738 paragenesis of aggregates. Comparison of (b) and (c) shows that each tiny V^0
739 inclusion represents the end of a long rod or dendrite branch.

740

741 Figure 5. Hibonite-grossite aggregate illustrating crystallization sequence. (a-e)
742 resorbed corundum in hibonite reflects peritectic reaction $L + Cor \rightarrow Hib$, followed by
743 grossite+ spinel \pm krotite; fluorite and $Ca_4Al_6F_2O_{12}$ crystallize last. V^0 appears to
744 separate from melt at temperatures near the peritectic reaction, as few inclusions of
745 V^0 are found in the corundum; (f) aggregate showing late crystallization of the F-
746 bearing perovskite phase; (g-h) BSE image and phase distribution map showing
747 intergrowth of perovskite and fluorite. Dark grey phase in BSE image is ?gibbsite,
748 which replaces fluorite and leaves geode-like open cavities.

749

750 Figure 6. (a) Phase map of aggregate showing randomly-oriented hibonite plates,
751 with narrow resorbed corundum cores, and hibonite+grossite intergrowths at edges
752 of plates. Grossite (light green) is euhedral against CaF_2 (orange), the last phase to
753 crystallize. Spinel (blue-green) are euhedral. (b) Element-distribution maps for Ca
754 and Al.

755

756 Figure 7. Parageneses of vanadium “balls”. (a) vanadium spheroids with spinel,
757 grossite and fluorite; (b) BSE image of spheroid #1 in (a), showing intergrowth of Mn-
758 rich and Mn-poor V; (c) BSE image and map of V distribution in spheroid #2 in (a),

MS 66733R revised 28-09-2018

759 showing intergrowth of native V with V-Mn alloy; (d) V spheroid partially altered to
760 unidentified Ca-V phase(s).

761

762 Figure 8. High-Al (mean 15 wt%) V balls in nest of grossite between hibonite laths,
763 with outlines suggesting they were fluid when trapped. Note euhedral $\text{Ca}_4\text{Al}_6\text{O}_{12}\text{F}_2$
764 protruding into fluorite, the last phase to crystallize. The coexistence of $\text{Ca}_4\text{Al}_6\text{O}_{12}\text{F}_2$
765 with grossite and fluorite constrains the crystallization of the assemblage to $>1150\text{ }^\circ\text{C}$
766 (Kim, 2011); see Fig. SD5.

767

768 Figure 9. 3D- μCT images of dendritic native V in hibonite. (a) low-resolution image
769 of two dendrite clusters in a hibonite grain. (b) magnified view, looking parallel to
770 (0001) face; red to orange, vanadium; green, open cavities; (c) view from starting
771 point, toward crystal face along *c* axis. Tendrils radiate off irregular clumps of V^0 .
772 Some consist of a series of joined balls that extend toward the crystal surface, then
773 sprout into 3-D dendritic networks with clear breaks and restarts at intermediate
774 crystal planes. The patterns suggest nucleation of V melts on the surface of growing
775 crystals. (See animated version in Figure SD3).

776

777 Figure 10. Chondrite-normalized trace-element abundances. (a) hibonite in hibonite-
778 grossite aggregates; (b) mean hibonite in aggregates vs mean hibonite included in
779 corundum; (c) coexisting hibonite-grossite pairs, linked by colour.

780

781 Fig 11. Phase diagrams constraining temperatures of crystallization. (a) two “end-
782 member” versions of the $\text{CaO-Al}_2\text{O}_3$ binary, showing reactions as eutectics (Guo et
783 al., 2015; black lines) or peritectics (Jerebtsov and Mikhailov, 2001; red lines); red
784 star shows average bulk composition of hibonite-grossite aggregates (Table 1); (b)
785 Al-corner of $\text{CaO-MgO-Al}_2\text{O}_3$ liquidus diagram (after data from FactSage);
786 intermediate Ca-Mg-Al oxides (1-4) have not been identified in this study.

787

788 Figure 12. $\text{CaO-Al}_2\text{O}_3\text{-SiO}_2$ liquidus diagram at 1 atm. pressure (after Osborne and
789 Muan, 1960; Gentile and Foster, 1963), showing compositions of hibonite-grossite-
790 spinel aggregates, and calculated and analysed melts; red arrows show the effects
791 of desilication, and crystallization of hibonite+grossite aggregates.

792

MS 66733R revised 28-09-2018

793 Figure 13. Calculated liquidus diagrams of CaO-Al₂O₃-SiO₂ system at 3 pressures,
794 after Ottonello et al. (2013). Trd/Cr, tridymite/cristobalite; Qz, quartz; Wo,
795 wollastonite; An, anorthite; Mul, mullite; Rk, rankinite; Gh, gehlenite; Crn, corundum;
796 Hbn, hibonite; Gros, grossite, Grs, grossular; Krt, krotite; Lrn, larnite. Note the
797 shrinkage of the fields of anorthite and gehlenite, and the expansion of the krotite
798 and hibonite fields, with increasing P, and disappearance of the liquidus field of
799 grossite above ca 1 GPa.

800

801 Figure 14. Analyzed glasses and calculated melts. (a) trace-element spectra of
802 melts calculated using distribution coefficients of Kennedy et al. (1994; K94), and the
803 analyzed glass coexisting with hibonite in Paragenesis A; (b) trace-element spectra
804 of glasses described in text; (c) comparison of calculated melts with hibonite-bearing
805 glasses from Lance and Murchison meteorites (Ireland et al., 1991).

806

807 **Tables**

808 Table 1. Major-element compositions of selected phases, and bulk aggregates

809

810 Table 2. Trace-element compositions of selected phases

811

812 Table 3. Calculated melts and estimated partition coefficients

813

814

815 **Supplementary Data**

816 Figure **SD1**. Location map showing position of the study area within the Levant-
817 Arabia context (a) and geological map (b) with sample localities. Volcanic centres on
818 Mt Carmel are marked by yellow dots.

819

820 Figure **SD2**. Aggregate showing apparent quench structure; thin hibonite tablets
821 radiate from coarse crystals of grossite + spinel, suggesting crystallization from a
822 substrate into liquid.

823

824 **Figure SD-3**. 3D-CT video of vanadium dendrites in hibonite crystal. Red-orange,
825 vanadium; green, open cavities.

826

827 **Figure SD4**. Interelement correlations in V-rich spinels of paragenesis B.

MS 66733R revised 28-09-2018

828

829 **Figure SD5.** CaF_2 - CaAl_2O_4 binary (after Kim, 2011) showing crystallization of
830 $\text{Ca}_4\text{Al}_6\text{F}_2\text{O}_{12}$ from ca 1500 °C to 1390 °C, and instability of $\text{Ca}_4\text{Al}_6\text{F}_2\text{O}_{12}$ + grossite +
831 CaF_2 below ca 1150°C. Red arrow shows possible evolution of the late melts in the
832 hibonite-grossite-spinel aggregates.

833

834

835 **Methods**

836

837 Samples were mounted in epoxy blocks, polished and coated with carbon. A Zeiss
838 EVO MA15 scanning electron microscope (SEM) at the Geochemical Analysis Unit
839 (GAU), Macquarie University, Sydney, Australia was used to capture Backscattered
840 Electron (BSE) images and Energy Dispersive X-ray spectrometry (EDS) was used
841 to map the elemental composition of the samples. An accelerating voltage of 15 keV
842 and a beam current of 1 nA was used.

843 Major elements were determined by electron microprobe (EMP) using a CAMECA
844 SX100 equipped with five wavelength-dispersive spectrometers at the Macquarie
845 University GeoAnalytical (MQGA; formerly GAU), Macquarie University, Sydney,
846 Australia. Analyses were performed using a focused beam (1-2 μm) with an
847 accelerating voltage of 15 keV and a beam current of 20 nA. Standards were a suite
848 of natural and synthetic minerals. Peak counting varied between 10 – 20 s, and
849 background was counted for 5 – 10 s on either side of the peak. Oxygen and carbon
850 were measured directly; matrix corrections were carried out by the ZAF software.

851 Major elements also were determined by electron microprobe (EMP) using a JEOL
852 8530F electron microprobe equipped with five wavelength dispersive spectrometers
853 at the Centre for Microscopy Characterisation and Analysis (CMCA), The University
854 of Western Australia, Perth, Australia. Analyses were performed using a fully
855 focussed beam with an accelerating voltage of 15 keV, a beam current of 15 nA.
856 Standards were a suite of natural and synthetic minerals. On-peak counting times
857 were 30 seconds for all elements. X-ray intensity data was corrected for Time
858 Dependent Intensity (TDI) loss (or gain) using a self-calibrated correction for Si $k\alpha$,
859 Ti $k\alpha$, Mn $k\alpha$, Na $k\alpha$, K $k\alpha$ and mean atomic number (MAN) background corrections
860 were used throughout (Donovan & Tingle, 1996; Donovan et al., 2016). Unknown

MS 66733R revised 28-09-2018

861 and standard intensities were corrected for deadtime. Oxygen was measured, matrix
862 corrections and ZAF correction were applied throughout.

863 Trace elements were obtained using a Photon Machines Excite 193 nm ArF
864 EXCIMER laser system coupled to an Agilent 7700x ICP-MS at the GAU, Macquarie
865 University, Sydney, Australia. Detailed method descriptions have been given by
866 (Jackson et al., 2004). The ablation conditions included beam size (50 μm), pulse
867 rate (5Hz) and energy density (7.59 J/cm²). Ablation was performed in an HelEx II
868 cell and helium was used as the carrier gas at a total flow rate of 0.825L/min.

869 Average analytical runs comprised of 20 analyses, 2 analyses of reference materials
870 and 10 analyses of unknowns, bracketed by two analyses of NIST610 standard glass
871 at the beginning and end of each run. Analyses consisted of 60 second of
872 background and 120 seconds of ablation. Trace element concentrations were
873 calculated from the raw signal data using the on-line software package GLITTER
874 ((Griffin et al., 2008); www.mq.edu.au/GEMOC). GLITTER calculates the element
875 concentrations and relevant isotopic ratios for each mass sweep and displays them
876 as time-resolved data. This allows homogeneous segments of the signal to be
877 selected for integration. GLITTER then corrects the integrated ratios for ablation-
878 related fractionation and instrumental mass bias by calibration of each selected time
879 segment against the identical time-segments of the standard glass (NIST610 using
880 the GeoReM values). An appropriate major element was used as an internal
881 standard to quantify trace element concentrations and the synthetic BCR2 and
882 NIST612 glasses were used as reference materials (GeoReM).

883 FIB foils from the region of interest were prepared for TEM using a dual- beam FIB
884 system (FEI Nova NanoLab 200). High Angle Annular Dark Field Scanning
885 Transmission Electron Microscopy (HAADF- STEM) imaging and element mapping
886 were carried out using an FEI Titan G2 80- 200 TEM/STEM with ChemiSTEM
887 Technology operating at 200 kV at the Centre for Microscopy Characterisation and
888 Analysis (CMCA), The University of Western Australia, Perth, Australia. The element
889 maps were obtained by energy dispersive X- ray spectroscopy using the Super- X
890 detector on the Titan with a probe size ~ 1 nm and a probe current of ~ 0.25 nA. Total
891 acquisition times of 20- 30 minutes were used to obtain good signal- to- noise ratios.
892 Electron diffraction was carried out using a field limiting aperture that selected an
893 area approximately 400nm in diameter.

MS 66733R revised 28-09-2018

894 For X-ray micro-computed tomography (μ CT), the grain was mounted on a finger of
895 rigid PVC plastic with double-sided tape and a separate tomogram was collected for
896 each grain using a μ CT system (Versa 520 XRM, Zeiss) running Scout and Scan
897 software (v11.1.5707.17179, Zeiss) at the CMCA. Samples were scanned at 50 kV
898 and 77 μ A with the source detector positions set to -17.7 and 117 mm, respectively.
899 An LE1 source filter was applied to screen out low energy X-rays. A 0.4X objective
900 lens was used together with 2x camera binning to achieve an isotropic voxel
901 resolution of 9 μ m. Each scan comprised 2501 projections through 360 $^\circ$ with an
902 exposure of 3s for each projection. Raw data were reconstructed using
903 XMReconstructor software (v11.1.5707.17179, Zeiss) following a standard centre
904 shift and beam hardening correction. The standard 0.7 kernel size recon filter setting
905 was also used. The visualization and analysis of data generated from μ CT scans
906 were performed using Avizo (v8.1.1, FEI) software
907

Table 1. EDS and EMP analyses of selected phases

wt%	hibonite							
	hibonite in corundum				hibonite in aggregates			
	SEM-EDS		EMP		SEM-EDS		EMP	
	n=24	stdev	n=6	stdev	n=48	stdev	n=13	stdev
SiO ₂	0.43	0.38	0.16	0.12			0.03	0.04
ThO ₂			0.15	0.05				
ZrO ₂	0.59	0.59	0.46	0.26				
HfO ₂								
Ti ₂ O ₃	2.95	1.59	2.61	1.5			0.02	0.02
Al ₂ O ₃	83.2	1.38	82.8	4.52	90.1	0.72	89.80	0.99
Cr ₂ O ₃	1.00	0.56					0.02	0.01
La ₂ O ₃	0.19	0.1	n/a					
Ce ₂ O ₃	1.18	1.16	3.46	2.9				
Sc ₂ O ₃			0.01	0.02				
P ₂ O ₅								
Y ₂ O ₃			0.06	0.05				
VO			0.01	0.01	0.90	0.71	0.60	0.39
FeO			0.01	0.01				
MnO			0.06	0.06				
MgO	2.07	0.21	1.88	0.65	0.51	0.20	0.66	0.19
CaO	6.49	0.74	5.78	1.56	8.31	0.15	8.30	0.11
F							0.20	0.05
C								
Totals	98.07		97.45		99.82		99.63	

Atomic Prop.

Si	0.15		0.06	0.04				
Th			0.01	0.004				
Zr	0.10		0.08	5				
Hf								
Ti	0.78		0.79	0.41				
Al	34.40		35.4	1.13	36.9	0.25	37.31	0.56
Cr	0.26							
La	0.02							
Ce	0.15		0.47	0.40				
V					0.21	0.16	0.17	0.11
Fe								
Mn			0.02	0.02				
Mg	1.04		1.02	0.37	0.31	0.11	0.35	0.1
Ca	2.45		2.23	0.55	3.10	0.06	3.13	0.06
F							0.20	0.10
O	60.65		59.9	0.52	59.4	0.14	58.91	0.56

c

|

||

||

grossite				spinel					
				w/ Hbn+Crn	high-V spinel			medium-V-spinel	
SEM-EDS		EMP		SEM-EDS	EMP		EMP		
n=41	stdev	n=12	stdev	n=1	n=9	stdev	n=10	stdev	
		0.01	0.01		0.04	0.02			
78.5	0.26	77.02	0.47	3.9 72.1	0.40 60.92	0.50 1.96	0.03 69.84	0.03 1.2	
					1.40	0.18	0.22	0.08	
		0.10	0.12						
		0.15	0.10		16.41	2.60	3.95	1.01	
				3.0	3.68	2.55	0.86	0.41	
21.4	0.18	0.05 21.24	0.02 0.18	20.6	19.75	0.89	23.95	0.63	
					0.25	0.06	0.2	0.04	
99.9		98.57		99.6	102.85		99.05		
						0.02	0.01		
33.3	0.09	0.01 33.0	0.01 0.39	1.13 29.43	0.13 29.30	0.16 0.15	29.63	0.77	
					0.47	0.00			
		0.05	0.02		6.27	0.99	1.21	0.4	
				0.88	1.31	0.91	0.26	0.12	
8.30	0.07	8.21	0.11	10.63	12.16	0.48	12.85	0.22	
					0.11	0.03	0.07	0.03	
58.4	0.03	58.7	0.49	57.92	50.55	1.52	58.0	0.51	

|| | |

low-V spinel		perovskite		Ca ₂ Al ₆ O ₁₃ F ₂		fluorite		
EMP		EMP		EMP		SEM-EDS		EM
n=10	stdev	n=3	stdev	n=10	stdev	n=20	stdev	n=6
0.02	0.03							
		1.78	0.2					
0.12	0.28	48.00	0.29					
71.81	0.84	2.68	0.09	54.3	1.1			
0.02	0.02	0.15	0.01					
		0.39	0.01	0.40	0.04			0.68
0.24	0.27	1.58	0.03					
		0.01	0.01					
0.46	0.39	0.11	0.02	0.04	0.04			
26.90	0.83			26.9	0.83			
0.18	0.05	39.49	0.20	38.2	0.6	50.6*	0.74	51.34*
		1.27	0.14	6.54	0.11	43.3		46.71
						5.43		
99.8		95.46		99.56		100.0		98.7

* Ca wt %

		0.39	0.05					
		17.45						
29.33	0.32	1.43	0.05	24.3	0.42			
0.01	0.01	0.05	0.01					
0.07	0.07	0.58	0.01					
		0.01	0.01					
0.13	0.11	0.04	0.01	0.01	0.01			
13.90	0.42							
0.07	0.02	19.23	0.16	15.55		35.4		34.16
		1.83	0.21	7.85		63.8		65.57
58.27	0.06	58.87	0.4	52.11	0.29			

| || || || 11.3 |

		Zr-Ti oxides						
		(Zr,Al)TiO ₃		Zr ₃ TiO ₇		ZrTiO ₃		(Zr,Ti
IP	stdev	SEM-EDS		SEM-EDS		SEM-EDS		SEM
		n=5	stdev	n=8	stdev	n=12	stdev	n=12
		1.01	1.54					
		49.1	5.41	66.1	4.33	78.2	1.53	92.3
		0.24	0.54	0.43	0.64	1.38	0.25	1.48
		34.4	2.66	25.2	2.43	16.2	1.31	4.68
		3.33	1.64	2.89	1.70	0.89	0.16	0.21
		2.03	1.85	0.86	0.18	0.27	0.49	
	0.02							
				1.50	1.34	0.48	0.39	
		1.33	0.7	0.77	0.37	0.44	0.17	
	1.36	3.26	2.15			0.68	0.27	0.13
		94.7		97.8		98.5		98.8
		0.70	0.97					
		15.2	1.83	23.7	2.07	29.4	1.02	37.2
				0.09	0.13	0.20	0.16	0.35
		18.3	1.37	15.5	1.17	10.5	0.84	3.27
		2.48	1.21	2.34	1.37	0.81	0.14	
				0.58	0.78	0.31	0.25	
		1.33	0.33	0.63	0.31	0.51	0.19	
	0.71	2.21	1.45	0.55	0.15	0.56	0.22	0.11
	0.72							
		58.5	1.59	56.2	0.69			

||

||

||

||

)203		Vanadium				Vana	
		SEM-EDS		EMP		V9(M)	
-EDS		n=28	stdev	n=5	stdev	n=4	stdev
	Si	0.49	0.48	0.42	0.22	0.67	0.25
	Ti						
2.78	Zr						
0.23							
1.39				0.01	0.02		
0.29	Al			0.32	0.5	4.28	0.1
	Cr	1.60	0.39	1.6		0.71	0.77
	V	96.2	1.3	95.2	3.23	88.7	2.83
	Fe			0.03	0.01		
	Mn	1.53	0.99	1.21	0.63	5.12	1.92
	Mg						
0.18	Ca	0.19	0.22	0.09	0.06	0.54	0.41
		100.0		98.9		100.0	

0.59
0.06
0.91
0.16

||

dium n,Al)		V4Al				reconstructed aggregates
EMP		SEM-EDS		EMP		n=9
n=5	stdev	n=7	stdev	n=7	stdev	
0.52	0.11	0.43	0.06	0.38	0.04	0.02
0.01	0.01					
0.15	0.11			0.20	0.03	
3.94	1.27	11.8	0.40	11.58	0.25	79.5
0.71		0.44	0.50	0.44		
79.83	6.86	85.2	0.66	83.37	0.76	0.50
0.01	0.01					
12.20	6.55	2.19	0.39	2.09	0.07	
0.41	0.35			0.21	0.17	2.1
						16.2
						1.0
97.78		100.1		98.28		99.3

Table 2. Trace elements (LAM-ICPMS)

	Hibonite A		Hibonite B		Grossite B		Spinel B	
	mean	stdev	mean	stdev	mean	stdev	mean	stdev
	n=2		n=9		n=7		n=4	
Li	59.1		<1.5				7.46	0.98
Be	10.0		<0.2				<0.3	
B	19.2		30.0	16.7	27.9	19.0	29.9	5.83
Na	45		24.0	13.3	90.7	12.0	332	267
Mg	11863		3700	875	542	49	149364	14403
Si	4777		1302	540	1017	676	1135	185
P	3.4		55.1	23.6	31.6	22.4	55.8	14.4
K	104		<5		<5		48.2	63.2
Sc	171		<0.5		0.22	0.37	<0.7	
Ti	16777		291	206	58.4	32.1	152.3	24.3
V	1.8		6002	3358	1804	748	25517	2437
Cr	0.2		13.9	9.30	6.55	5.0	76.5	20.2
Mn	34		207	192	249	139	4361	1402
Fe	<20		67.4	23.1	166	49	<30	
Co	<0.1		<0.1		0.05	0.06	<0.2	
Ni	3.5		<0.5		0.24	0.26	<0.5	
Cu	<0.2		<0.2		0.01	0.02	<0.3	
Zn	0.02		<1		0.60	0.75	9.60	2.0
Ga	7.6		0.42	0.4	0.03	0.05	<0.2	
Rb	<0.5		<0.2		<0.15		<0.2	
Sr	9889		76.4	26.9	34.7	10.1	<7	
Y	407		3.10	0.6	3.89	0.77	0.06	0.01
Zr	3468		5.21	3.7	0.12	0.24	<0.1	
Nb	<0.1		0.12	0.1	<0.01		<0.05	
Cs	<0.1		<0.1		<0.01		<0.1	
Ba	153		10.8	3.7	6.18	1.31	1.54	2.1
La	5758		7.73	5.1	0.09	0.11	<0.04	
Ce	15222		20.7	16.5	0.24	0.29	<0.05	
Pr	1181		3.38	4.7	0.03	0.04	<0.04	
Nd	3716		5.80	4.0	0.07	0.20	<0.02	
Sm	493		1.45	1.2	0.09	0.08	<0.3	
Eu	54		0.22	0.1	0.09	0.03	<0.06	
Gd	277		0.69	0.5	0.06	0.09	<0.3	
Tb	30.7		0.14	0.2	0.02	0.02	<0.05	
Dy	136		0.55	0.3	0.31	0.15	<0.2	
Ho	19.9		0.11	0.2	0.05	0.05	<0.03	
Er	42		0.13	0.1	0.27	0.08	<0.1	
Tm	3.5		0.01	0.02	0.03	0.03	<0.04	
Yb	46		0.05	0.08	0.18	0.14	<0.2	
Lu	1.5		<0.03		0.02	2.00	<0.04	
Hf	227		0.21	0.2	0.01	0.02	<0.2	
Ta	<0.1		0.17	0.1	<0.01		<0.15	
Pb	<0.2		<0.12		<0.15		<0.2	

Th	2807		10.5	9.5		<.05			<0.04
U	443		2.35	1.2		0.04	0.01		<0.04

Table 3. Analyzed glasses and calculated melts

	Major Elements							
	hibonite in corundum n=24	Calc. Melt Kennedy	Calc. Melt this work	Melt analyzed n=6		hibonite in aggregates n=48	Calc. Melt Kennedy	Calc. Melt this work
SiO ₂	0.43	215	27.8	31.0	0.3		15	
ZrO ₂	0.59	1.5	2.5	0.4				
Ti ₂ O ₃	2.95	2.3	2.2	0.5	0.03		0.02	
Al ₂ O ₃	83.2	42	44.8	40.6	90.1	45	38	
Cr ₂ O ₃	1.00							
La ₂ O ₃	0.19	0.03						
Ce ₂ O ₃	1.18	0.24						
Sc ₂ O ₃				0.69				
V ₂ O ₅					0.90			
FeO								
MnO								
MgO	2.07	4.1	1.7	0.8	0.51	1.0	0.3	
CaO	6.49	20	21.0	19.2	8.31	26	21	
BaO				0.9				
SrO	0.6	0.8						
K ₂ O				3.2				
Na ₂ O				1.0				
SO ₂				0.7				
sum	98.7		100.0	99.0	100.2	72.0	73.7	

Trace elements

	Hbn in		Partition coefficients hibonite/melt				
	Crn n=2	agg n=8	Crn hi-Ce glass	agg hi-Ba glass	Kennedy	Ireland	Dr/Boyn
Li	59.1	<0.5	0.25				
Be	10.0	0.1	0.32	0.13			
B	19.2	34.0	0.005	0.003			
Na	45	24.8	0.018	0.002			
P	3.4	57.5	0.018	0.90			
K	104	15.2	0.100	0.012			
Sc	171	<0.2	0.67		0.31	1.4	
Ti	16777	238	0.20	0.071	1.25		
V	1.8	5092	0.010	128		0.30	
Cr	0.2	11	0.007	0.32			
Mn	34	159	0.082	7.08			
Fe	<20	70		0.078			
Co	<0.1	0.1		0.13			
Ni	3.5	0.8	0.098	0.047			
Cu	<0.2	<0.2					
Zn	0.02	1.02	0.000	0.001			
Ga	7.6	0.62	0.41	0.090			
Rb	<0.5	0.31		0.27			
Sr	9889	72.9	8.28	0.36	0.63	0.86	0.53
Y	407	3.10	0.53	0.041		1.1	
Zr	3468	4.32	0.35	0.000	0.36	1.2	
Nb	<0.1	0.13		0.03	0.18	0.19	
Cs	<0.1	0.08		0.66			
Ba	153	10.2	0.084	0.001	0.03	2.5	
La	5758	7.86	7.34	0.35	6.20	6.0	7.2
Ce	15222	20.5	9.66	0.46	5.15	4.5	
Pr	1181	3.55	7.63	0.76	4.35	4.5	
Nd	3716	5.80	6.65	0.35	3.55	4.0	
Sm	493	1.45	4.49	0.41	1.70	2.9	2.7
Eu	54	0.22	2.47	0.24	1.30	0.4	0.53
Gd	277	0.86	2.85	0.20	0.92	3.0	1.49
Tb	30.7	0.16	1.86	0.17	0.64	2.2	
Dy	136	0.54	1.18	0.061	0.38	1.4	
Ho	19.9	0.18	0.78	0.07	0.26	1.1	
Er	42	0.19	0.56	0.019	0.20	0.58	
Tm	3.5	0.04	0.30	0.022	0.12	0.34	
Yb	46	0.16	0.56	0.010	0.06	0.22	0.1
Lu	1.5	<0.2	0.13		0.04	0.22	
Hf	227	0.26	0.91	0.0004	0.73	4.0	
Ta	<0.1	0.15		0.30			

Pb	<0.2	<0.2			
Th	2807	9.75	3.94	0.41	1.15
U	443	2.14	3.29	0.11	0.07

meteoritic glasses with hibonite (Ireland et al., 1991)				Calculated melts - trace elements			
	Lance	Mur 7-228	Mur 7-753	melt with Hbn in Crn			melt w/ Kennedy
				Kennedy	Ireland	Dr/Boyn	Kennedy
SiO ₂	36.7	40.2	40.1				
Ti ₂ O ₃	1.3	1.6	2.7				
Al ₂ O ₃	29.2	27.7	27				
MgO	6.8	7.3	7.3				
CaO	25.5	22.9	22.6				
sum	99.5	99.7	99.7				
Trace elements							
Sc	81	37	6.6	552	122		
Ti				13421			190
V	848	864	1154		6		
Sr	307	37	27	15697	11499	18658	116
Y	18	28	2.7		370		
Zr	169	83	16	9633	2890		12.0
Nb	8.6	8.9	9.8				0.74
Ba	27	0.59	5.9	5116	61		341
La	6.4	1.8	0.25	929	960	800	1.27
Ce	17	5.6	1.2	2956	3383		3.98
Pr	2.5	0.86	0.16	271	262		0.82
Nd	13	4.7	0.71	1047	929		1.63
Sm	4.3	1.8	0.71	290	170	183	0.85
Eu	0.49	0.66	25	41	128	102	0.17
Gd	4.4	2.9	0.18	302	92	186	0.93
Tb	0.83	0.6	0.07	48	14		0.25
Dy	5.8	4.5	0.41	357	97		1.43
Ho	0.99	1.02	0.11	78	18		0.71
Er	2.8	4.3	0.41	209	72		0.94
Tm	0.45	0.76	0.26	30	10		0.36
Yb	3.0	5.9	3.4	761	208	457	2.61
Lu	0.16	0.89	0.08	39	7		
Hf	1.24	0.68		310	57		0.36
Th				2441			8.48
U				6336			30.6

analyzed glasses Mt Carmel			
hi-Ce glass		hi-Ba glass	
n=65	stdev	n=25	stdev
45.0	2.8	43.6	2.2
1.94	1.3	8.24	1.9
1.95	1.2	1.24	0.3
26.3	6.1	34.0	2.3
0.42	0.7		
1.72	1.3		
4.6	3.0	0.12	0.2
14.0	3.2	4.38	0.7
		4.04	0.5
1.22	1.2	0.41	0.1
0.41	0.3	3.76	1.1
1.34	0.9		
97.6		99.8	

n=6	n=22
239	14.7
31	1.1
4076	9928
2466	11672
189	64
1040	1319
256	34
84731	3357
175	40
28	34
418	23
3032	898
3.9	1.1
35	17
2.6	1.0
1035	1145
18.7	6.9
2.5	1.2
1194	204
763	75
9838	26409
13.0	3.8
0.14	0.12
1826	12920
785	22
1576	45.0
155	4.7
559	16.8
110	3.5
22	0.9
97	4.3
16	1.0
115	8.9
26	2.5
75	9.9
11	1.9
82	16.4
12	3.0
249	627
1.2	0.5

3.9	8.3
712	23.7
135	19.4

rts	
Hbn in aggregates	
Ireland	Dr/Boyn
16973	
85	138
2.8	
3.6	
0.70	
4.1	
1.31	1.09
4.56	
0.79	
1.45	
0.50	0.54
0.51	0.41
0.29	0.58
0.07	
0.39	
0.16	
0.32	
0.12	
0.71	1.56
0.07	

Figure 1

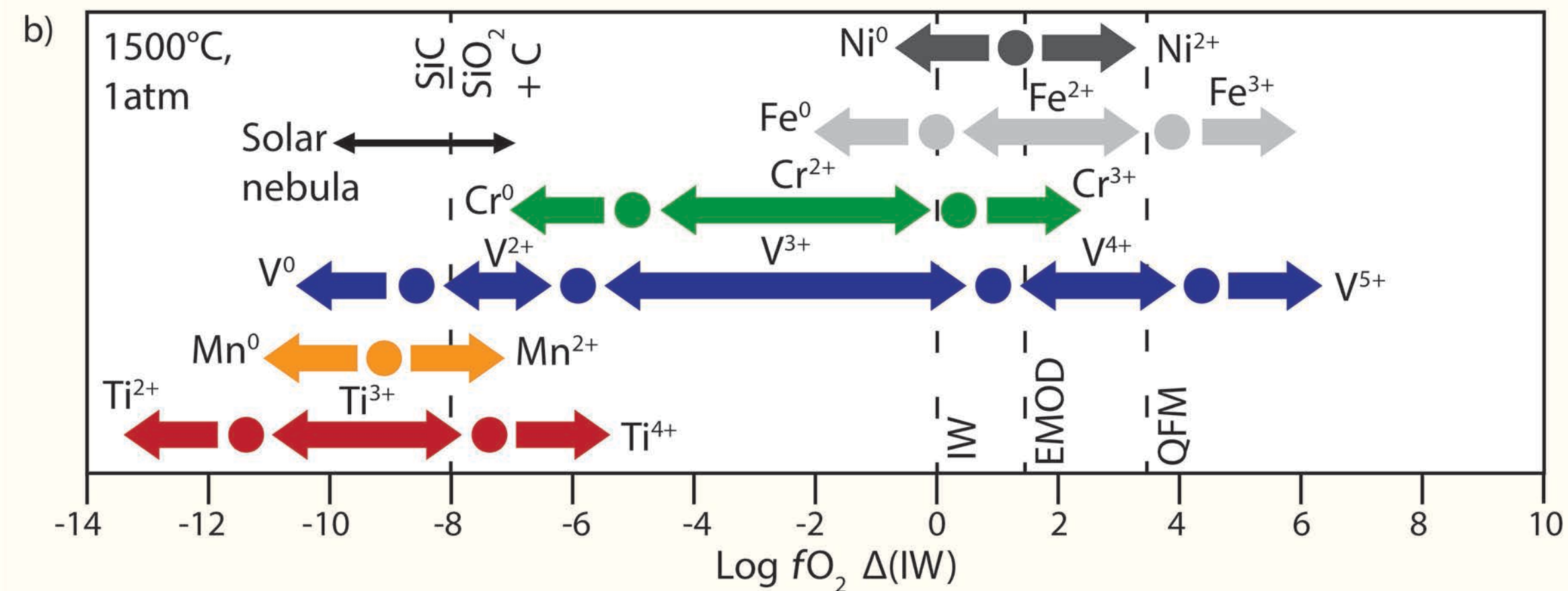
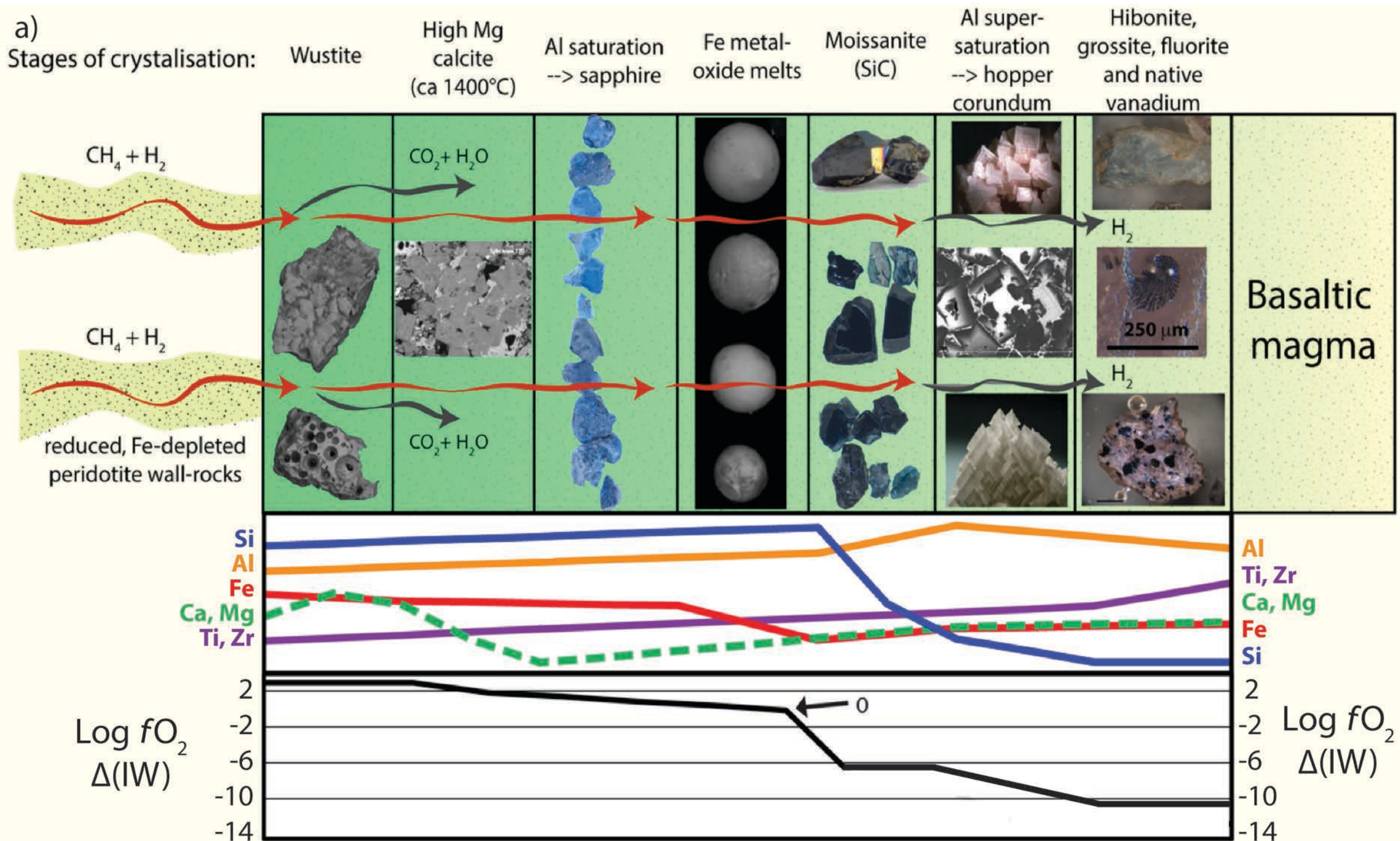


Figure 2

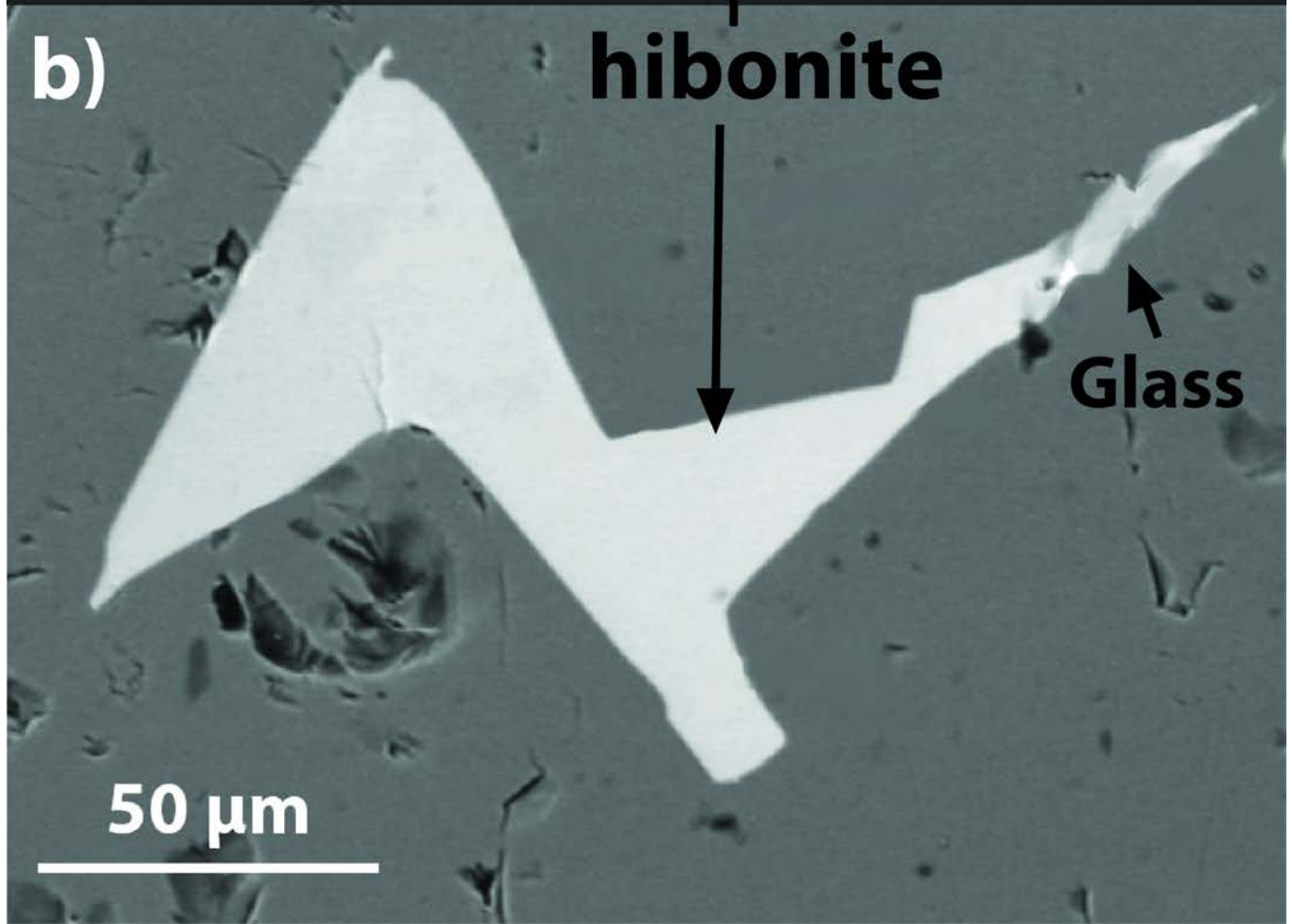
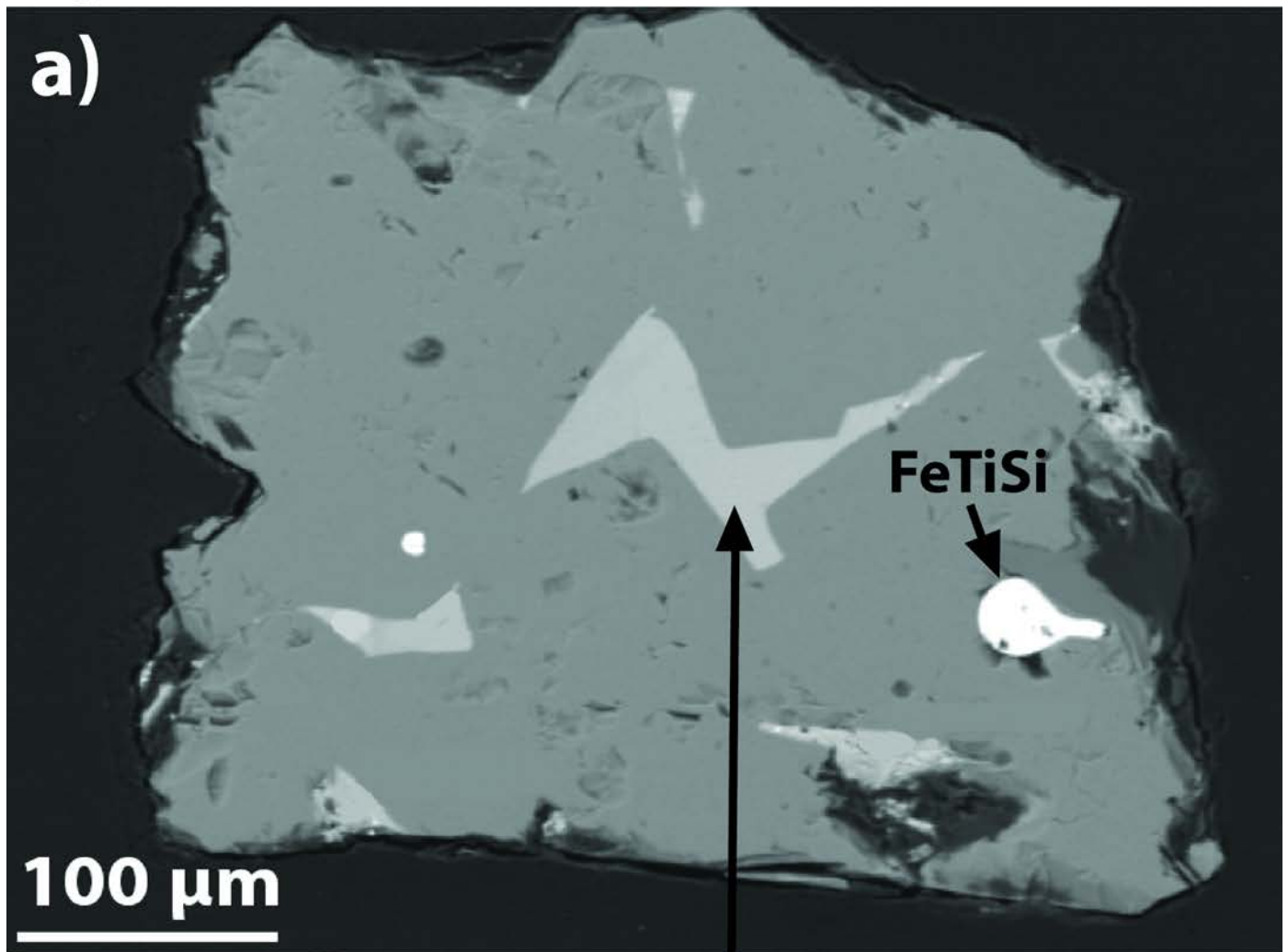


Figure 3

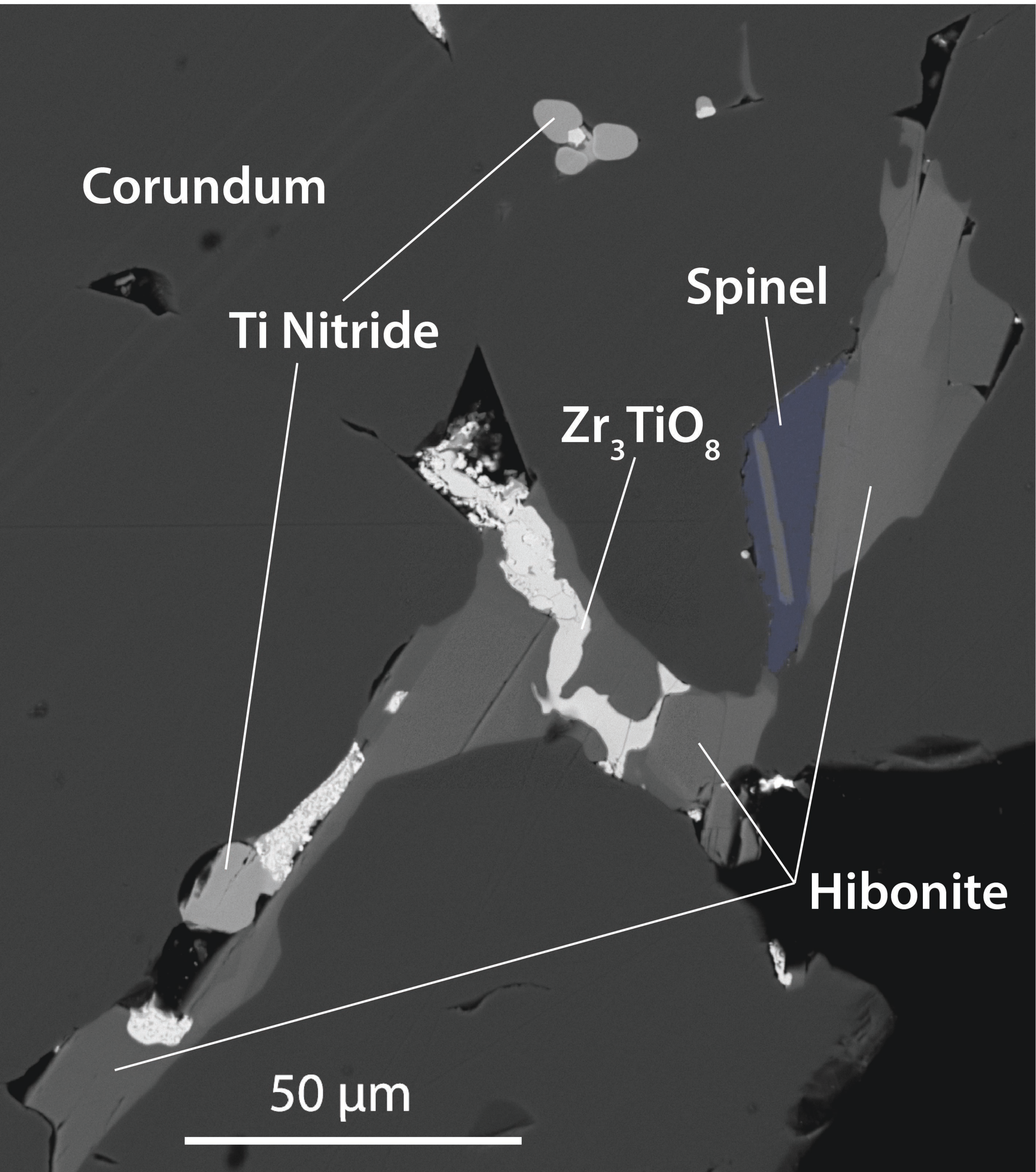


Figure 4

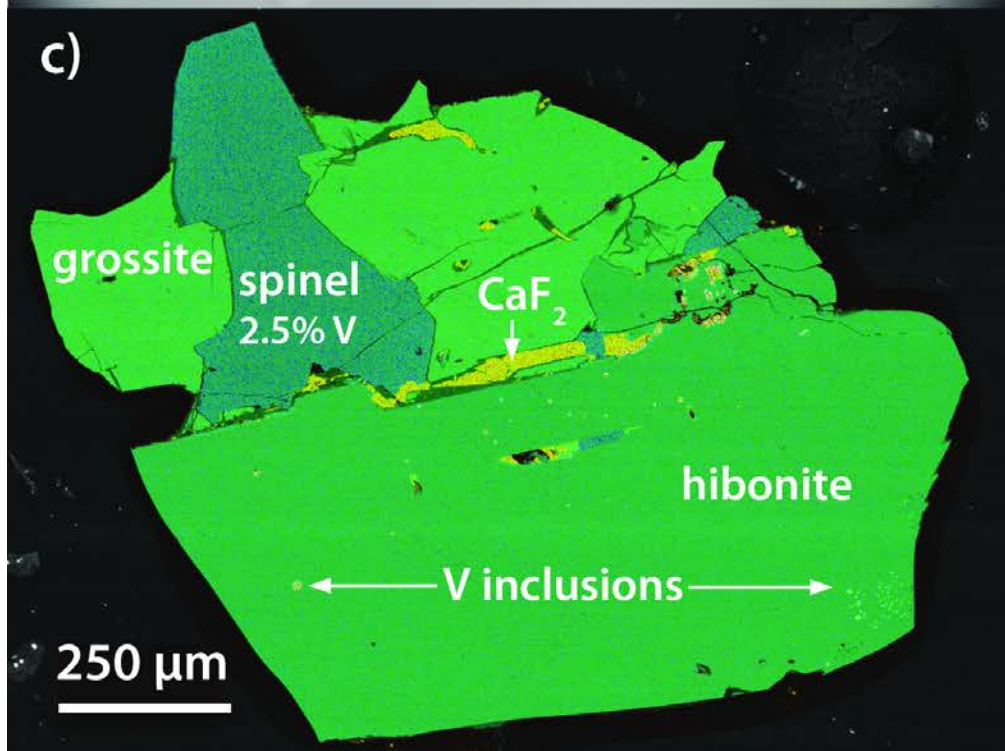
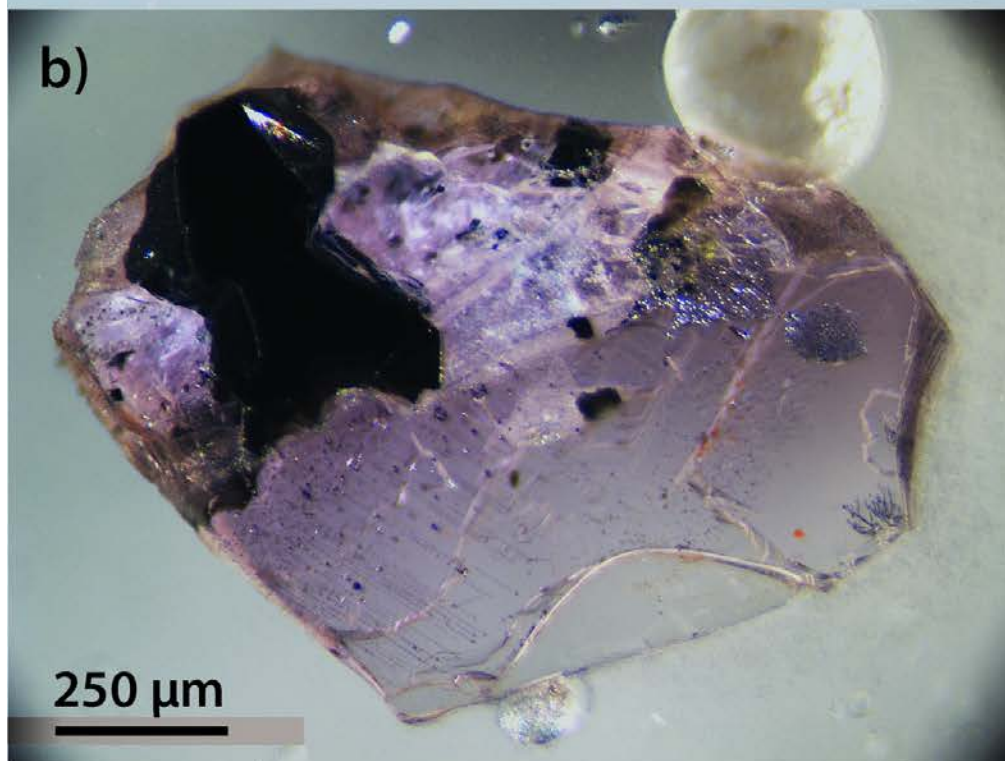
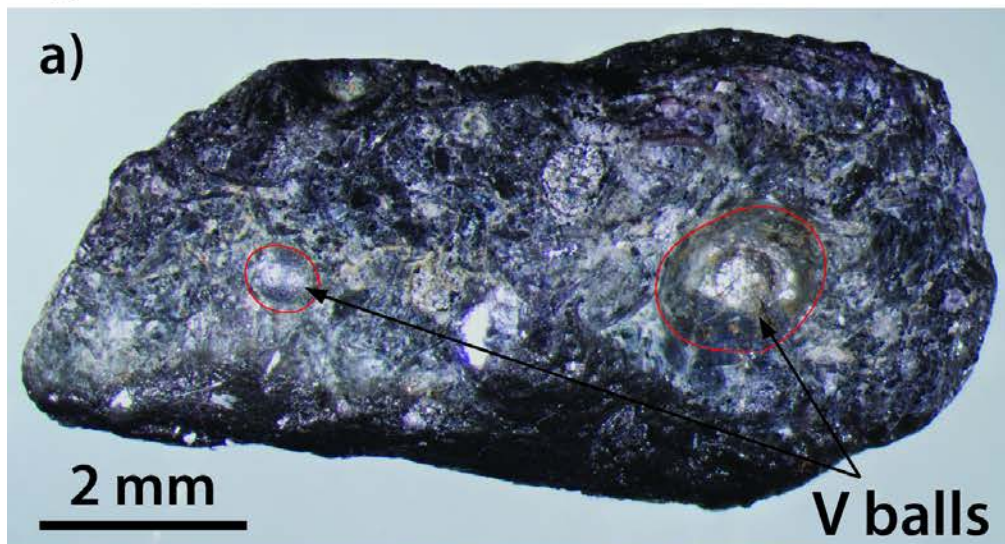


Figure 5

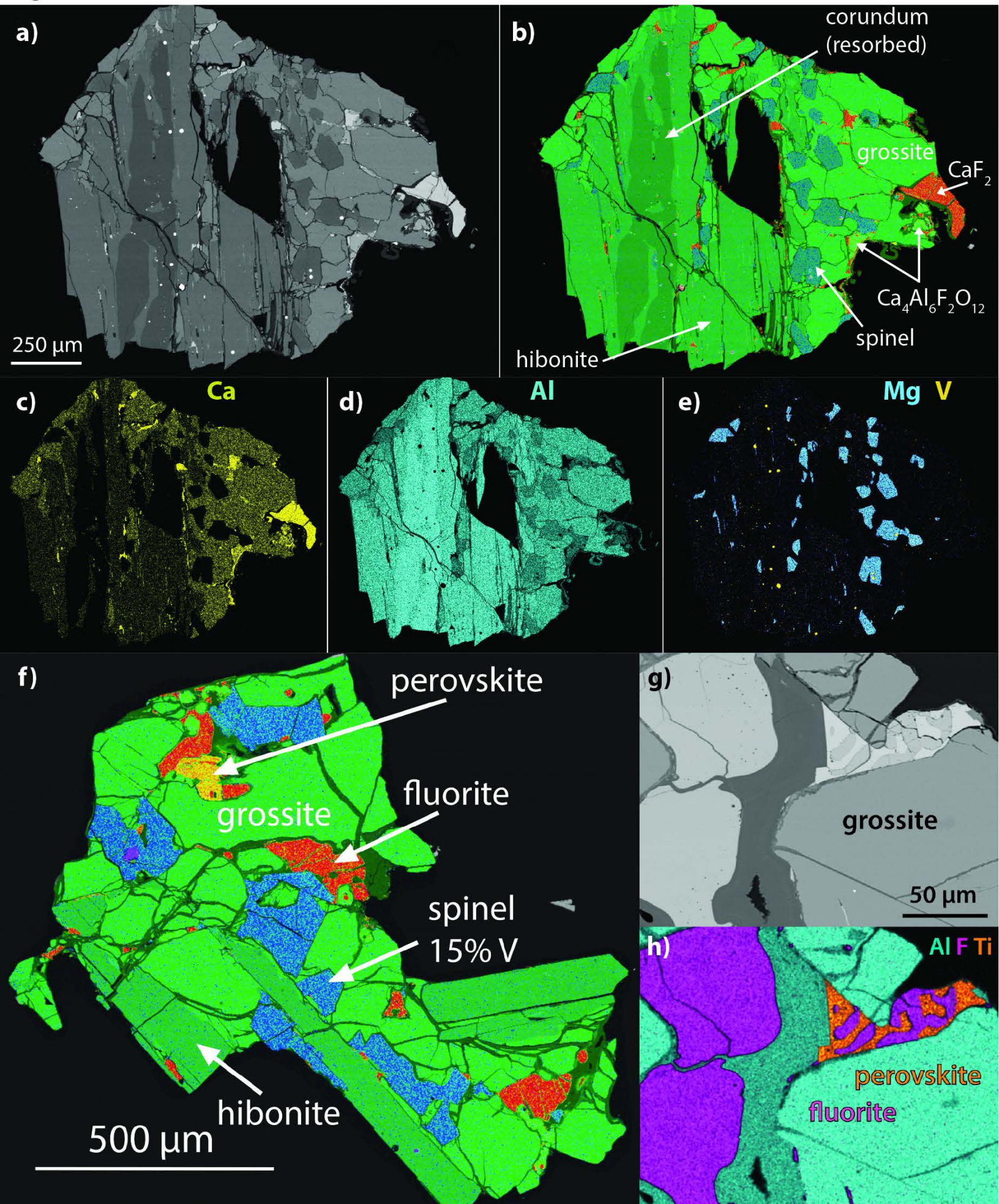
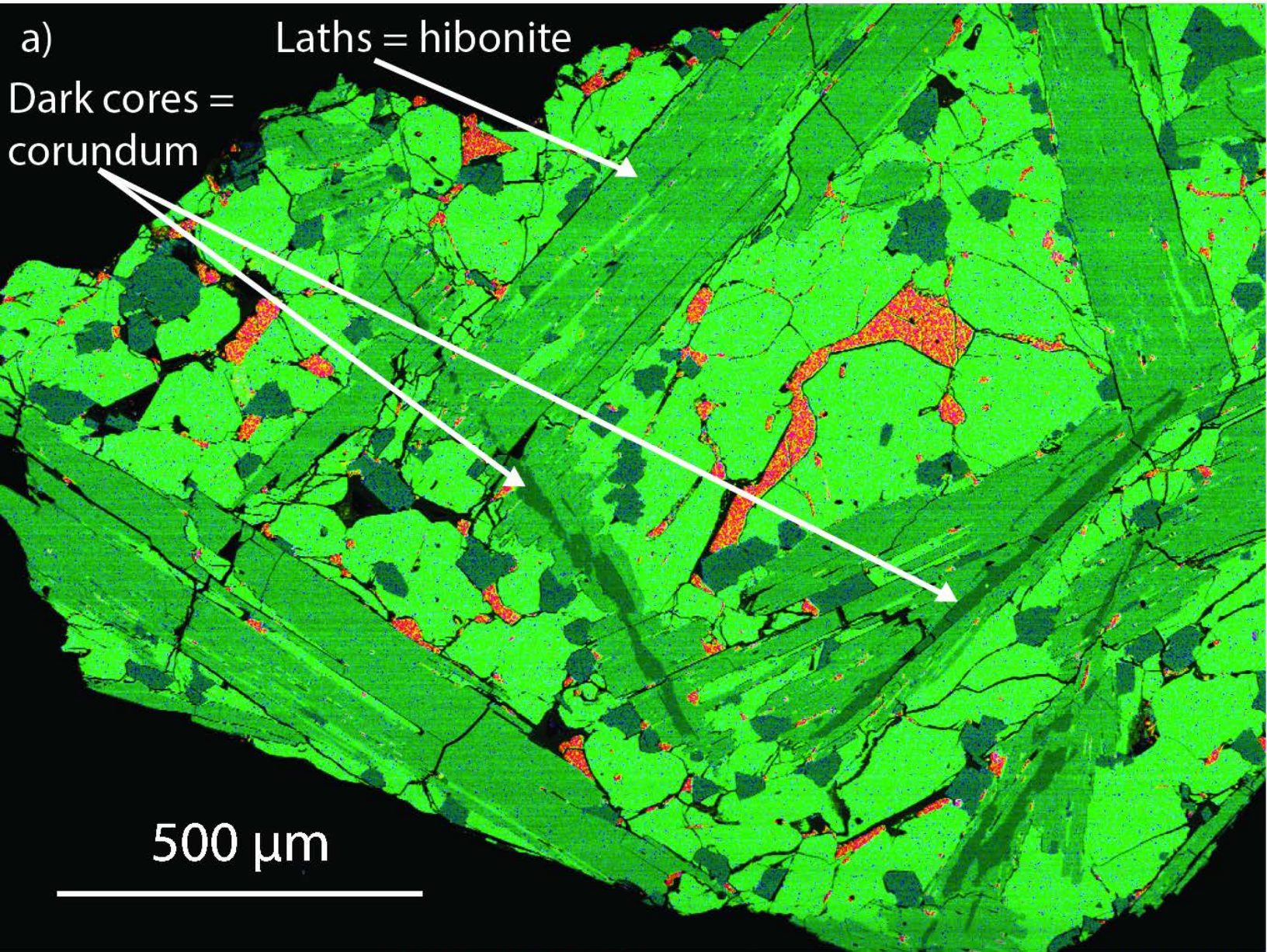


Figure 6

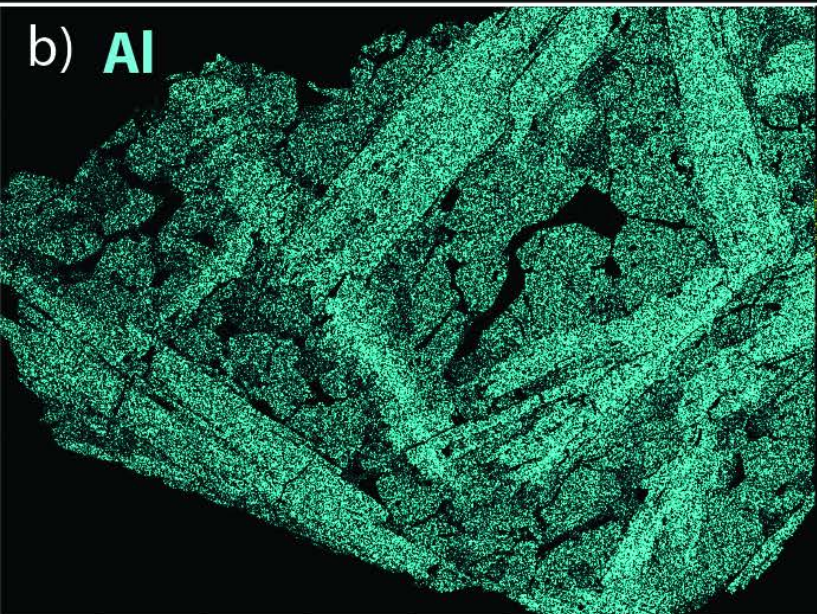
a) Dark cores = corundum

Laths = hibonite



500 μm

b) Al



Ca

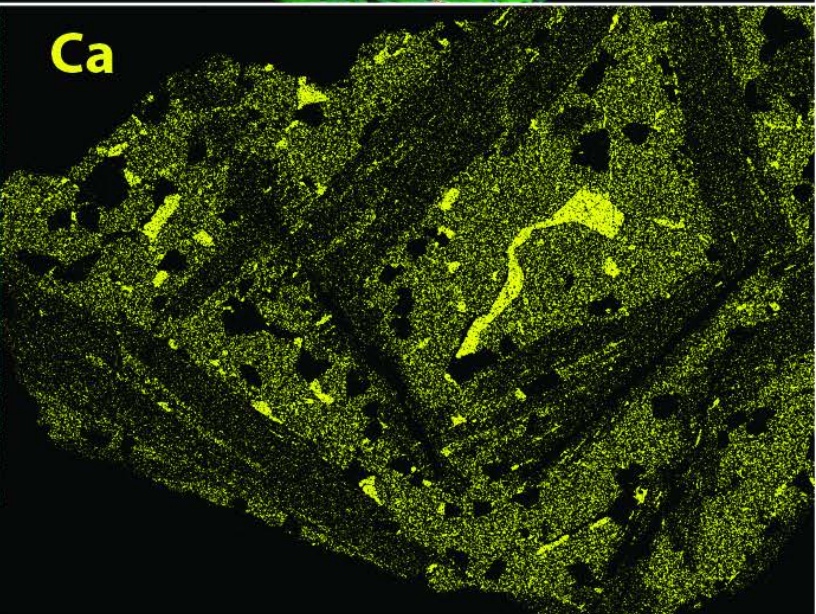


Figure 7

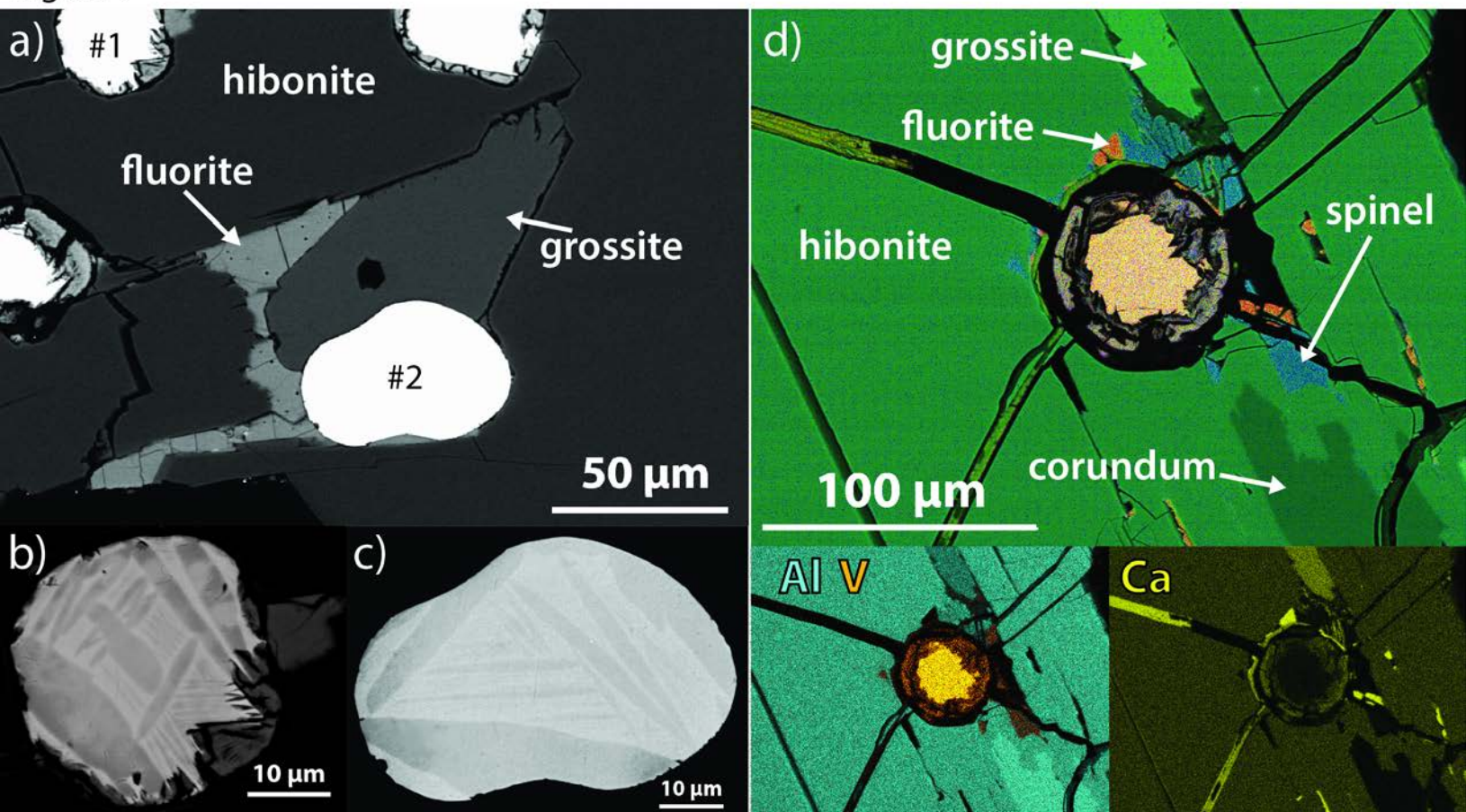


Figure 8

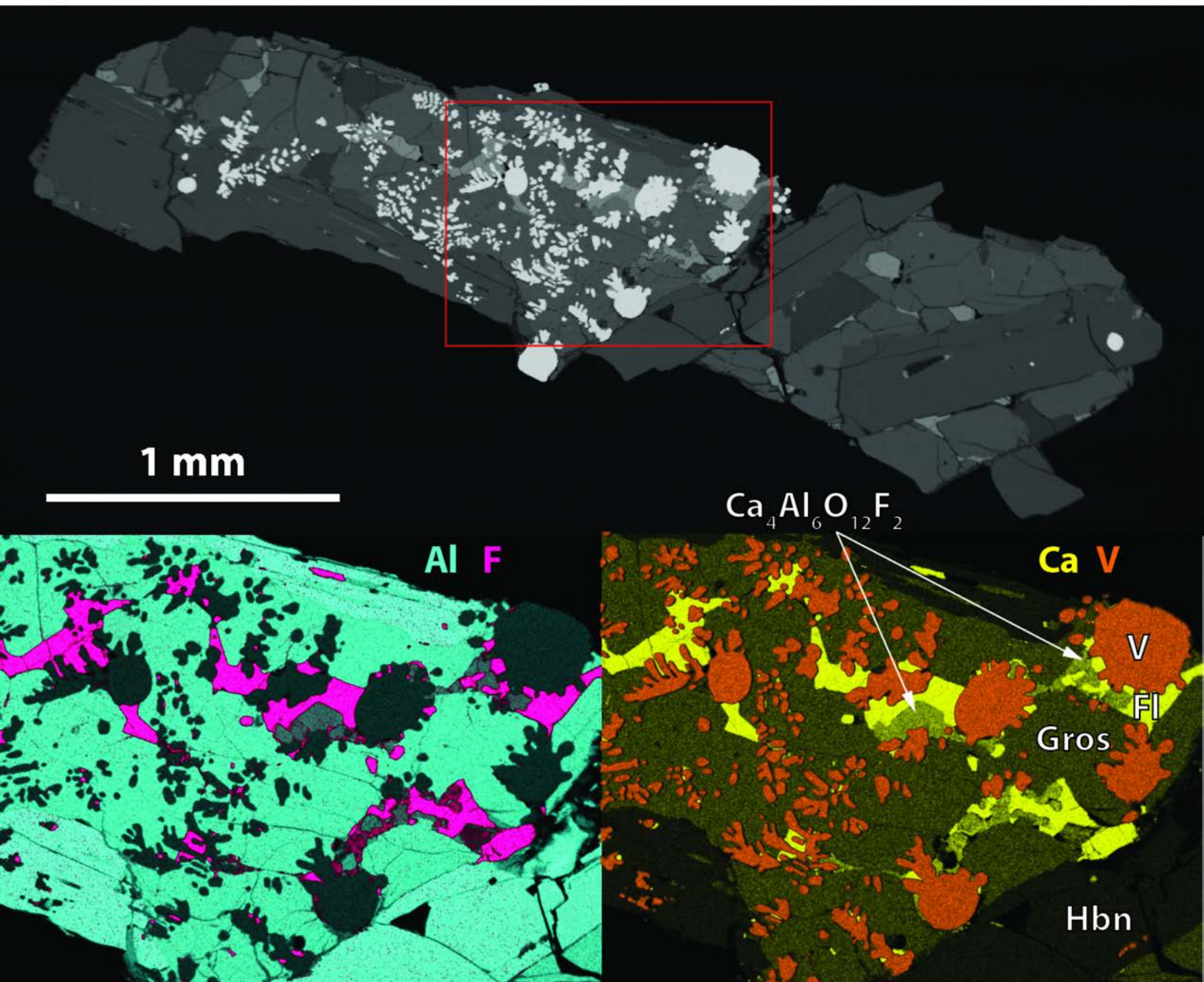


Figure 9

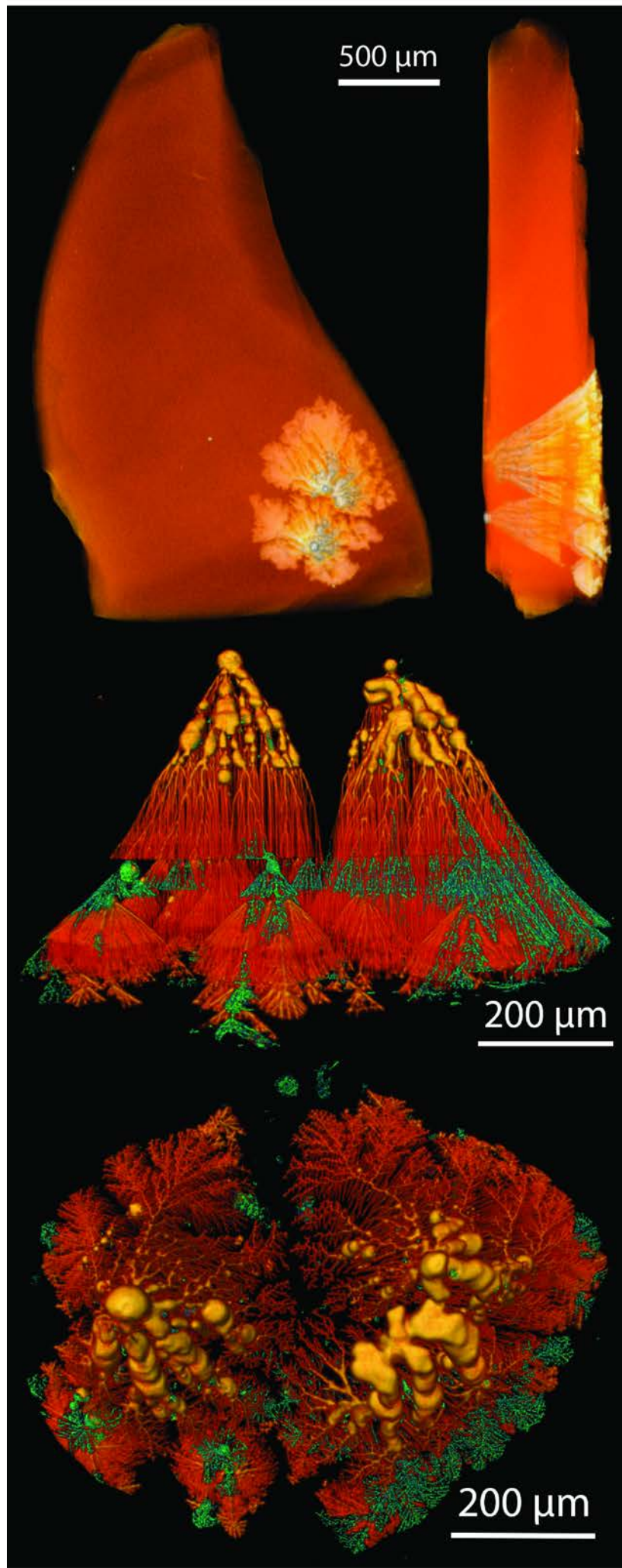


Figure 10

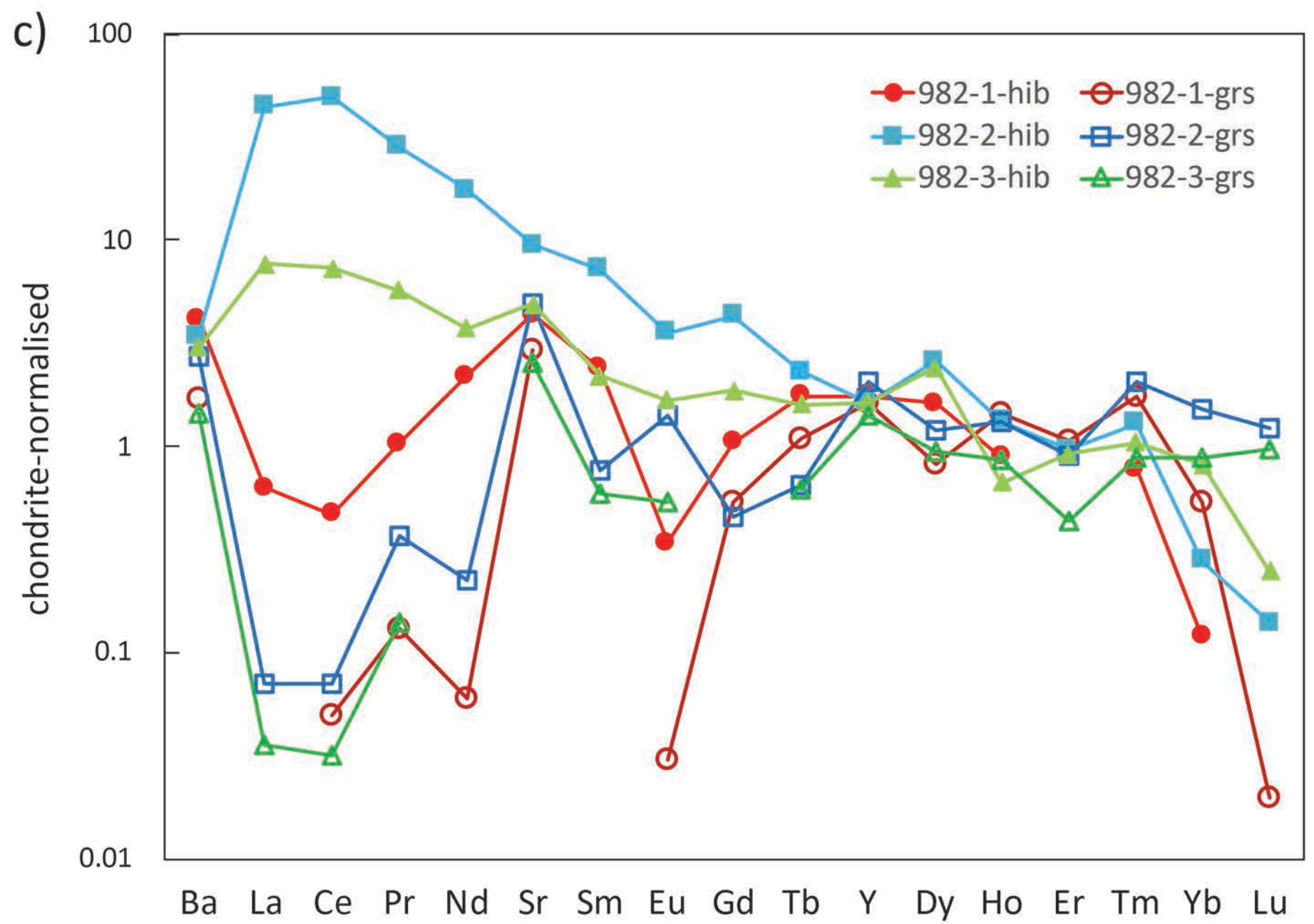
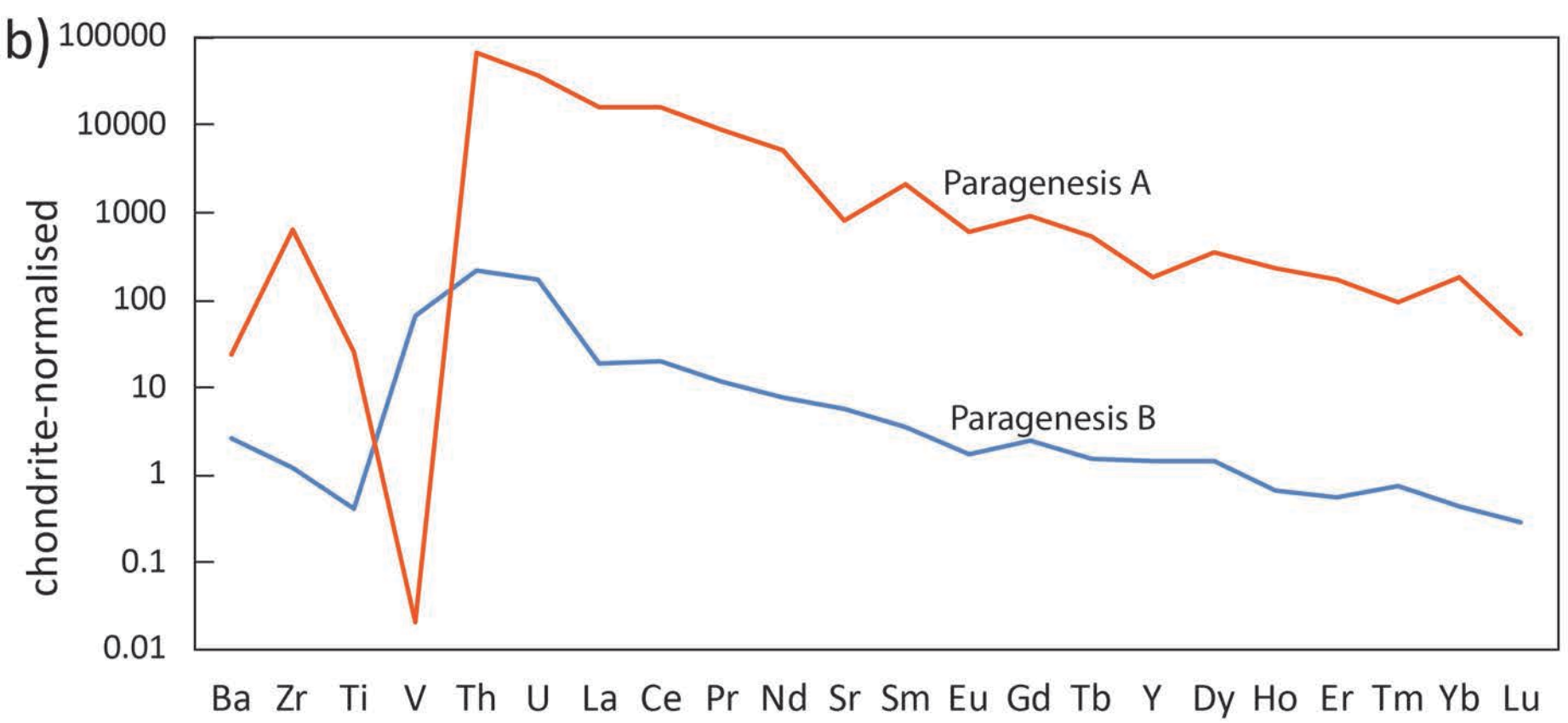
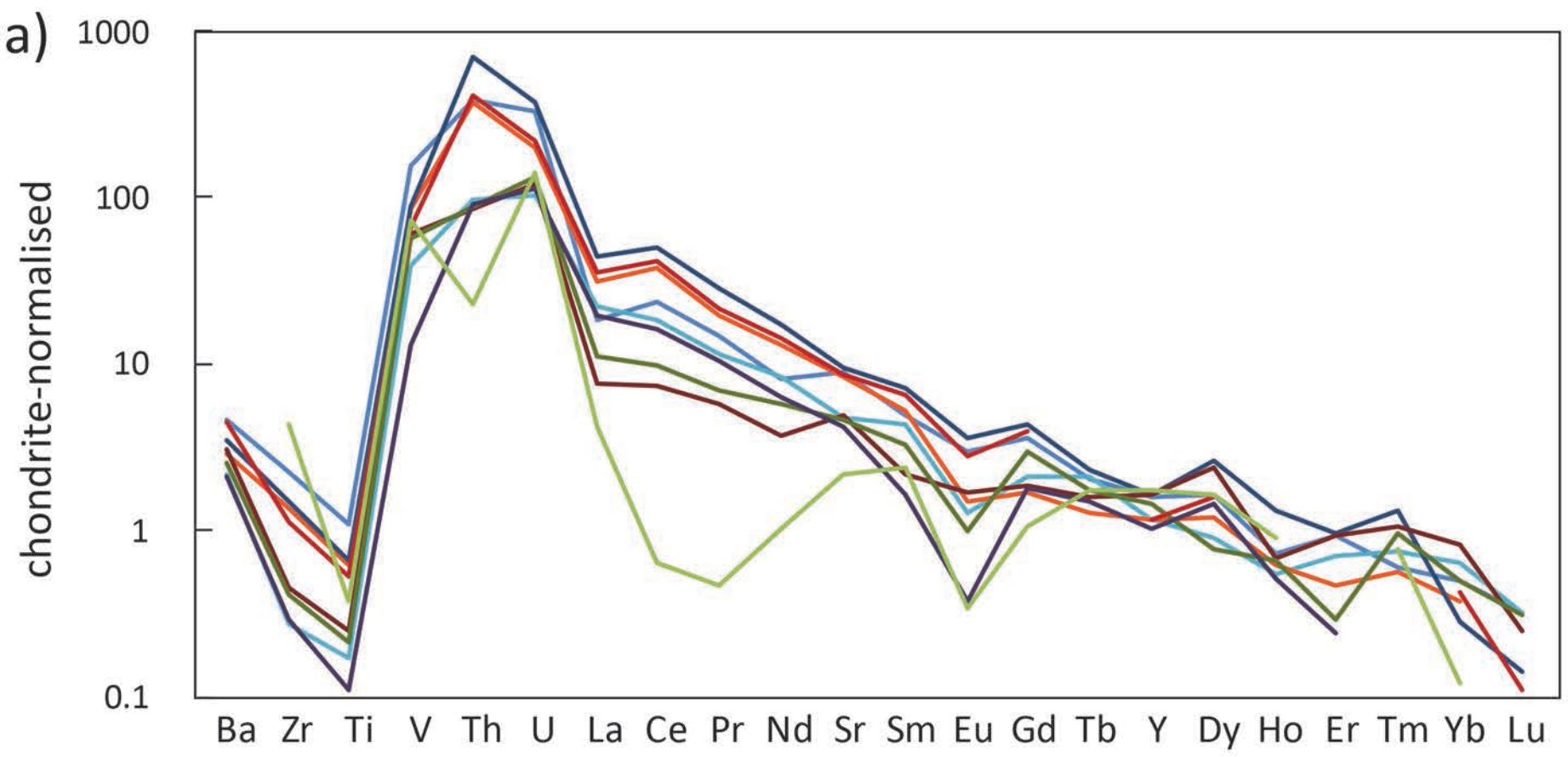


Figure 11

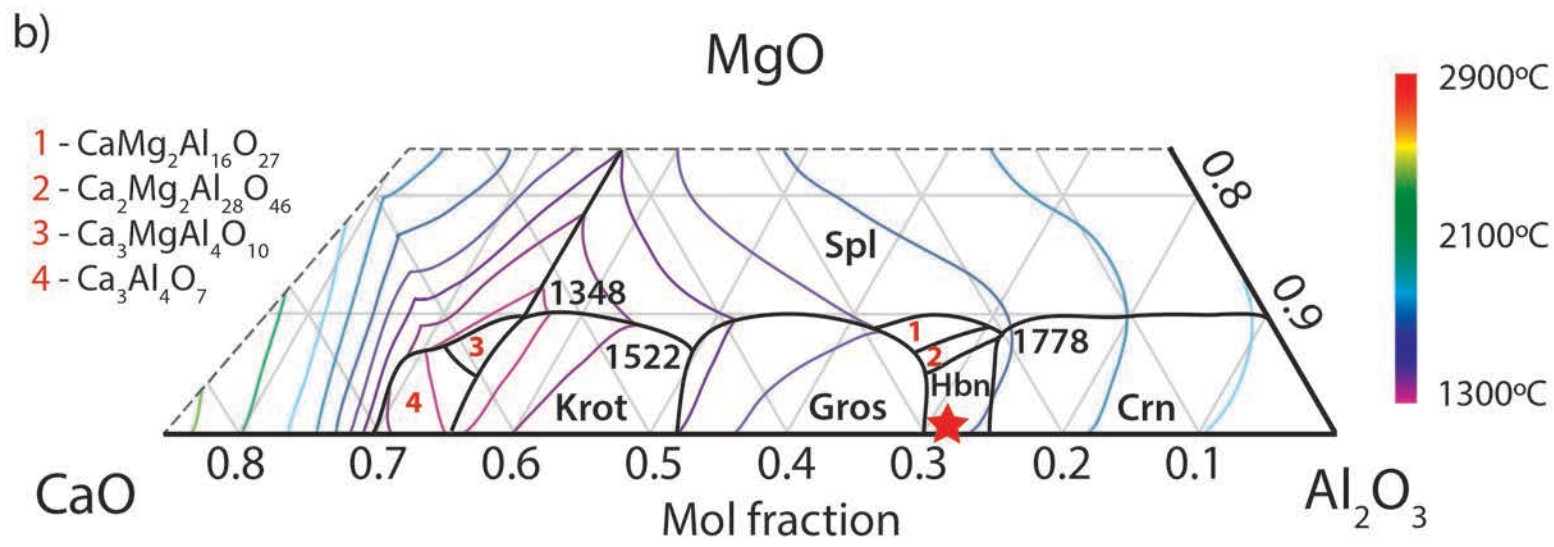
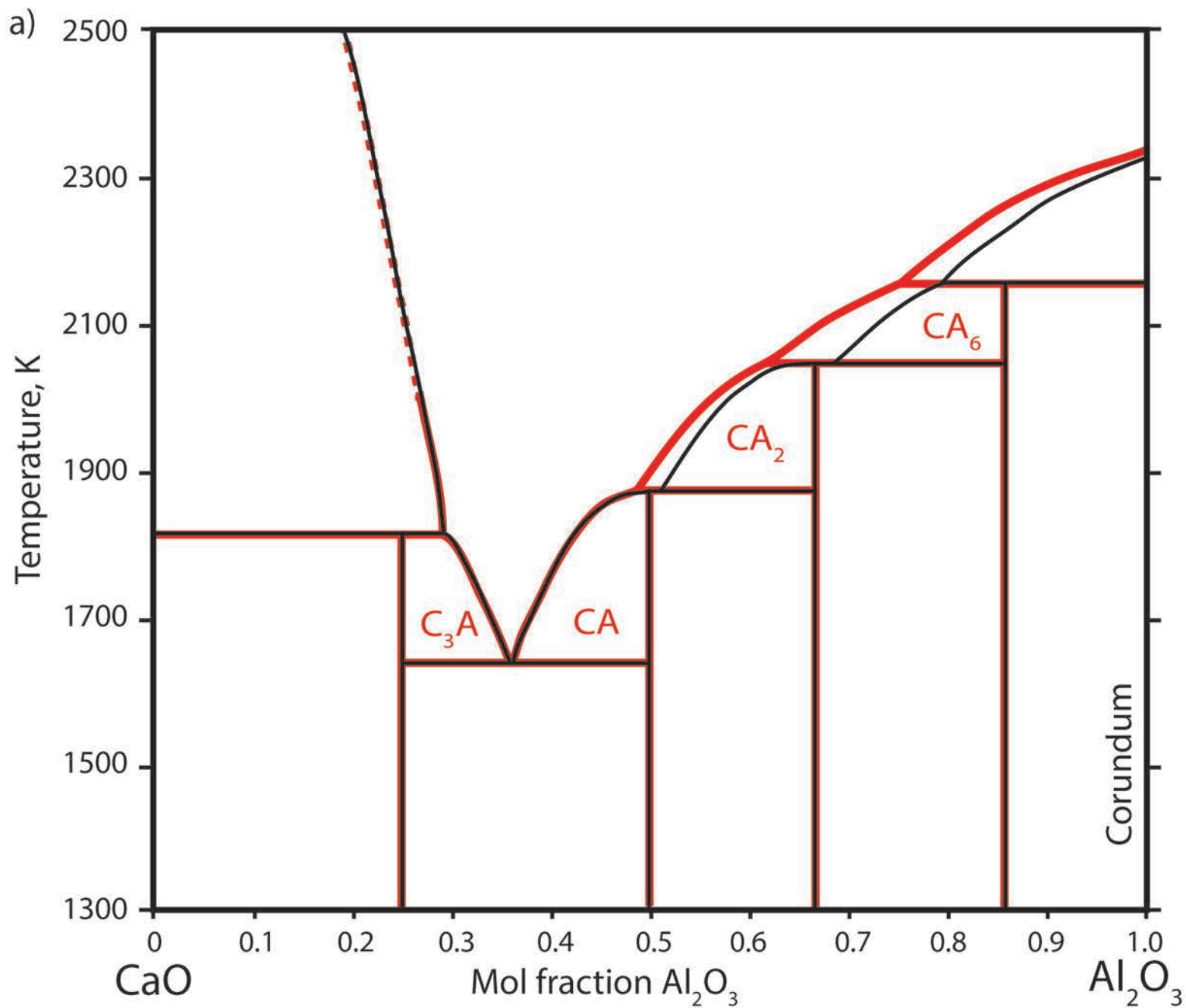


Figure 12

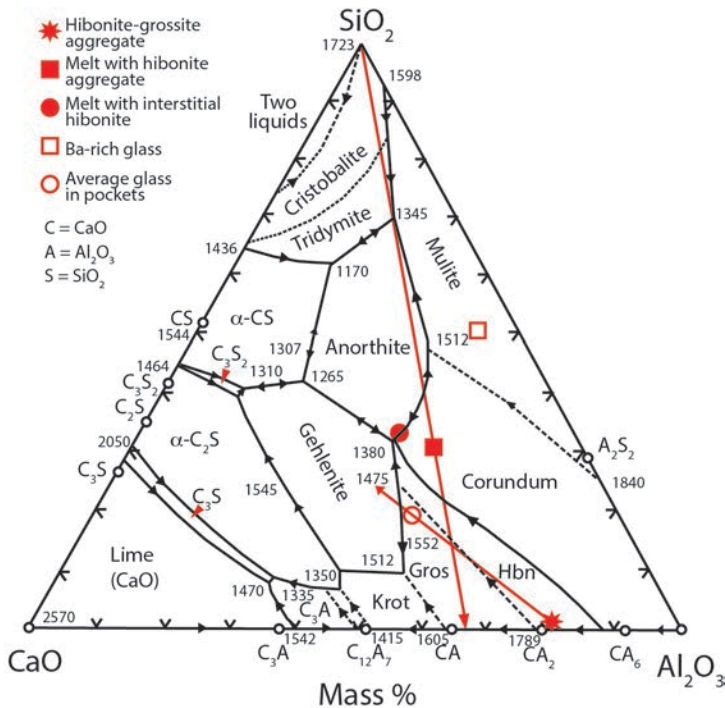


Figure 13

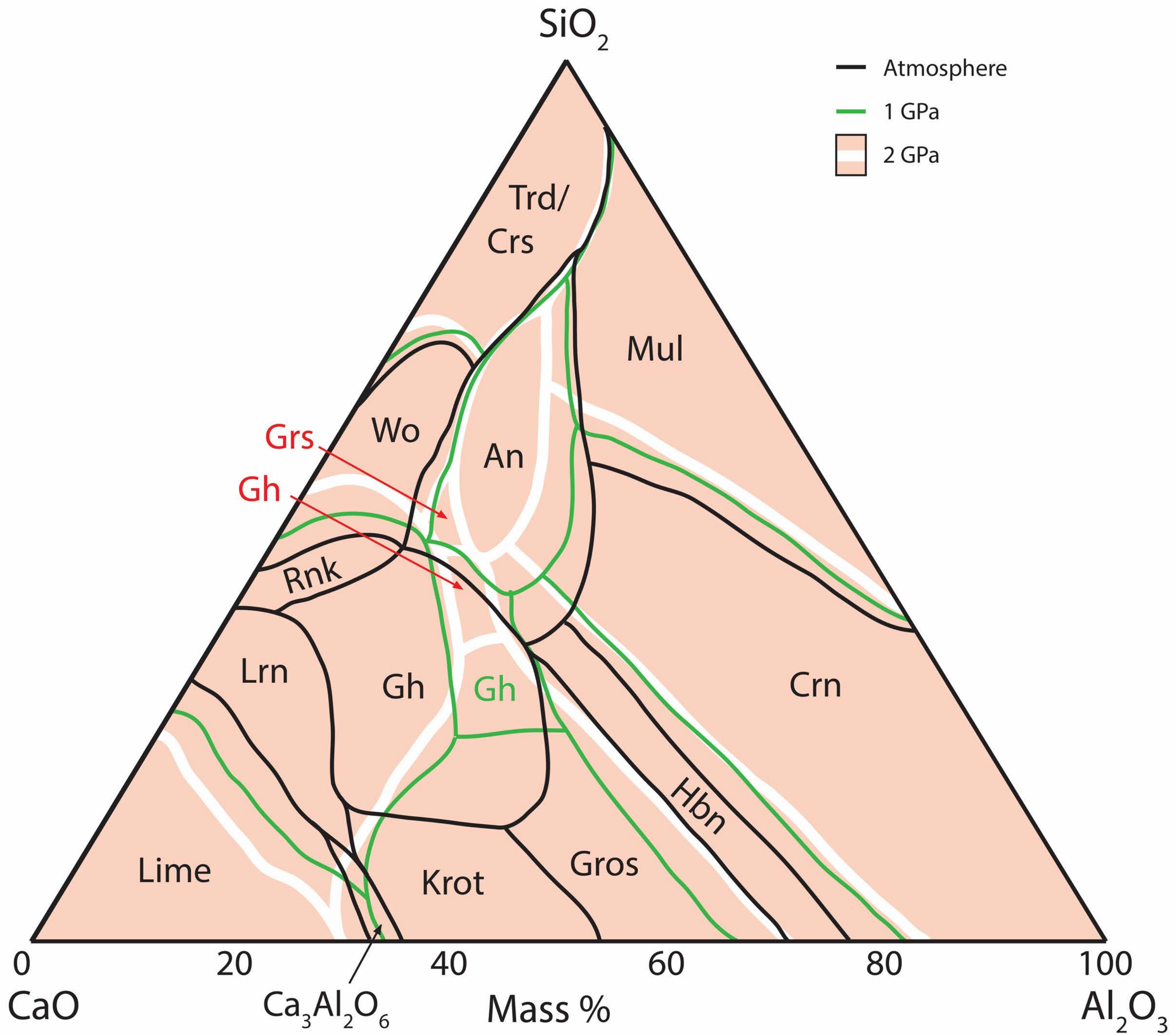


Figure 14

